

Cite as: J. H. Marshel *et al.*, *Science*  
10.1126/science.aaw5202 (2019).

# Cortical layer-specific critical dynamics triggering perception

**James H. Marshel<sup>1\*</sup>, Yoon Seok Kim<sup>2\*</sup>, Timothy A. Machado<sup>1,2\*</sup>, Sean Quirin<sup>1\*</sup>, Brandon Benson<sup>3</sup>, Jonathan Kadmon<sup>3</sup>, Cephra Raja<sup>2</sup>, Adelaida Chibukhchyan<sup>2</sup>, Charu Ramakrishnan<sup>2</sup>, Masatoshi Inoue<sup>2</sup>, Janelle C. Shane<sup>4</sup>, Douglas J. McKnight<sup>4</sup>, Susumu Yoshizawa<sup>5</sup>, Hideaki E. Kato<sup>6</sup>, Surya Ganguli<sup>3</sup>, Karl Deisseroth<sup>1,2,7,8†</sup>**

<sup>1</sup>CNC Department, Stanford University, Stanford, CA 94305, USA. <sup>2</sup>Department of Bioengineering, Stanford University, Stanford, CA 94305, USA. <sup>3</sup>Department of Applied Physics, Stanford University, Stanford, CA 94305, USA. <sup>4</sup>Boulder Nonlinear Systems, Lafayette, CO 80026, USA. <sup>5</sup>Department of Natural Environmental Studies, Graduate School of Frontier Sciences, University of Tokyo, Kashiwa 277-8564, Japan. <sup>6</sup>Department of Molecular and Cellular Physiology, Stanford University, Stanford, CA 94305, USA. <sup>7</sup>Department of Psychiatry and Behavioral Sciences, Stanford University, Stanford, CA 94305, USA. <sup>8</sup>Howard Hughes Medical Institute, Stanford University, Stanford, CA 94305, USA.

\*These authors contributed equally to this work.

†Corresponding author. Email: deissero@stanford.edu

Perceptual experiences may arise from neuronal activity patterns in mammalian neocortex. We probed mouse neocortex during visual discrimination using a red-shifted channelrhodopsin (ChRmine, discovered through structure-guided genome mining) alongside multiplexed multiphoton-holography (MultiSLM), achieving control of individually-specified neurons spanning large cortical volumes with millisecond precision. Stimulating a critical number of stimulus-orientation-selective neurons drove widespread recruitment of functionally-related neurons, a process enhanced by (but not requiring) orientation-discrimination task learning. Optogenetic targeting of orientation-selective ensembles elicited correct behavioral discrimination. Cortical layer specific-dynamics were apparent, as emergent neuronal activity asymmetrically propagated from layer-2/3 to layer-5, and smaller layer-5 ensembles were as effective as larger layer-2/3 ensembles in eliciting orientation discrimination behavior. Population dynamics emerging after optogenetic stimulation both correctly predicted behavior and resembled natural neural representations of visual stimuli.

Visual perception in mammals is correlated with neural circuit activity emerging in visual cortex, but it is not known why some activity patterns give rise to perceptual experiences, and others do not. While visual cortex could play a causal role initiating percepts (1–6), it has not been technologically possible to causally test the precise influence on perceptually-driven behavior of groups of individually-specified cells—either stimulated sequentially or as synchronously-activated multi-neuron ensembles distributed across anatomical layers or volumes.

Anatomical knowledge of rodent visual cortex at the cellular level may provide a foundation to guide investigation of the neural circuits mediating perception. Prior work has revealed clear relationships between visual encoding of single neurons and cellular interconnectivity patterns—both within layer 2/3 of primary visual cortex (V1) (7–11), and reciprocally between V1 and higher visual areas (12, 13). Within V1, monosynaptic connectivity, synaptic weights, and reciprocal connectivity are heightened between nearby layer 2/3 pyramidal neurons that share similar visual tuning in response to oriented visual stimuli. In combination with inhibitory

mechanisms, this arrangement may help selectively amplify or suppress specific signals important for visual processing (14–18), and may emerge via activity-dependent plasticity (10, 17, 19–21). The functional relationship between these architectures and the circuit dynamics that give rise to perceptually-guided behaviors remains unclear.

Single-neuron-resolution optogenetic control in vivo (22) could provide a critical new dimension, building upon the foundations of circuit anatomy and physiology to elucidate how cellular ensembles elicit perceptually-guided behaviors. However, despite considerable progress developing cellular-resolution optogenetic control (14, 23–26), it has not yet been possible to elicit behaviorally-defined percepts via optogenetic control of individually-defined neurons in any sensory cortex of behaving mammals. Here we have developed and applied tools suitable for fast optogenetic control over ensembles of many neurons spanning large volumes of cortex during visually-guided behavior in mice, finding that natural dynamics and associated behavior can be elicited by optogenetic recruitment of a critical number of individually defined percept-specific neurons.

## Results

### **Marine organism-based genomic screen for new classes of microbial opsin**

We screened the genomes of >600 marine microbial organisms for potential channelrhodopsins that jointly exhibit large photocurrents, high light-sensitivity, and spectral compatibility with robust fluorescent activity reporters. Screening based on crystal structure-derived knowledge of residues forming the cation-conducting channelrhodopsin (CCR) pore revealed ~1000 suitable new CCR-like sequences (27) (Fig. 1A). We optimized these sequences for mammalian expression and performed whole-cell patch clamp in cultured hippocampal neurons. From this screen, we discovered a promising marine opsin gene (named here ChRmine, after the deep red color carmine; from *Tiarina fusus*).

The new gene exhibited little similarity to previously known CCRs, in fact exhibiting more similarity to anion-conducting channelrhodopsin (ACR) and proton-pumping proteorhodopsin (PR) genes (Fig. 1B and fig. S1). Expression in cultured neurons gave rise to ~4 nA inward (excitatory) photocurrents driven by 585nm light (Fig. 1C, comparison with other opsins in figs. S2 and S3, A and B). The reversal potential of  $-5.64 \pm 1.39$  mV (Fig. 1D) revealed robust  $\text{Na}^+/\text{K}^+$  permeability ideal for driving spikes in neurons under typical physiological ion balance conditions, and recovery from desensitization in darkness was found to be an order of magnitude faster than for other red-shifted opsins (half-recovery time  $0.63 \pm 0.08$  s; fig. S2A). Along with increased effective power density (EPD50) for ChRmine ( $0.03 \pm 0.01$  mW/mm<sup>2</sup>, fig. S2B), these properties resulted in the capability of ChRmine to drive sustained spiking up to 40 Hz with red-shifted light (fig. S2C). ChRmine reliably induced spiking even with short red-shifted light pulses and at low irradiance values (100% spike success rate at 1 ms, 0.08 mW/mm<sup>2</sup>; Fig. 1, E to G, and fig. S3C).

### **Simultaneous optogenetics and imaging in cultured neurons**

To probe ChRmine's suitability for all-optical experiments, we compared with GCaMP6m in cultured neurons using wide-field one-photon stimulation and imaging (28). We observed much larger orange light-evoked GCaMP6m fluorescence signals in ChRmine-expressing neurons compared with other ChR-expressing cells at the same light-exposure duration (Fig. 1, H and I). ChRmine evoked faster rise and decay of GCaMP6m signals at both orange (585 nm; Fig. 1, H and J) and red (635 nm; fig. S2D) wavelengths. We also tested the pH dependence of opsin-mediated GECI signals at external pH 7.0, 7.2, and 7.4 and note CsChrimson use was associated with pH-dependent  $\text{Ca}^{2+}$  transients (29, 30). In contrast, no such effect was observed with ChRmine (fig. S2E).

We next performed whole-cell recording during ChRmine stimulation via two-photon (2P) spiral scanning over the soma. Both laser power (Fig. 1K) and illumination wavelength (Fig. 1L) characterization revealed ChRmine photocurrents suitable for 2P all-optical experiments. Additionally, we could reliably drive spike trains up to 30 Hz (Fig. 1, M and N). A key concern of using red-shifted ChRs is persistent blue-light-driven cellular excitation occurring during imaging. We therefore characterized ChRmine responses to blue light. With one-photon illumination, spikes were not elicited by 470 nm light, even over a broad range of light powers that reliably drove spiking at 585 nm (up to 100  $\mu\text{W}/\text{mm}^2$ ; Fig. 1G); likewise, the 2P imaging laser (at 920 nm) did not elicit spiking over a broad range of powers (Fig. 1, M and N, and fig. S3, E and F). Lastly, we observed sub-millisecond spike jitter of 2P light-evoked spikes ( $0.99 \pm 0.26$  ms; Fig. 1O).

### **Kilohertz control and readout of 3D ensembles over mm<sup>2</sup> domains in vivo**

The precise temporal response and low irradiance requirements of ChRmine motivated new optical hardware to leverage this opportunity for eliciting meaningful circuit dynamics of behavior. To gain optical access across large volumes of cortex for single-cell photostimulation and leverage kHz temporal precision, we designed, fabricated, and optimized a high-pixel-density (1536x1536 pixels) spatial light modulator (SLM) for high-fidelity NIR hologram generation at high-speed (MacroSLM; ~85% diffraction efficiency in 2 ms at  $\lambda=1064$  nm; materials and methods). We integrated this SLM into a microscope with custom optical elements and developed precise temporal sequencing protocols in order to address large volumes of cortex during single-cell, ensemble-scale photostimulation while simultaneously imaging local neural activity dynamics (materials and methods). To achieve temporal resolution in the kHz regime, we incorporated multiple SLMs along the same photostimulation path, enabling temporally-multiplexed ensemble stimulation (MultiSLM, Fig. 2A, figs. S4 to S7, materials and methods, supplementary text).

Mouse primary visual cortex (V1) was transduced with a single integrated ChRmine/GCaMP6m virus (AAV8-CaMKIIa-GCaMP6m-p2a-ChRmine-TS-Kv2.1-HA; materials and methods) (31). This dual opsin/GECI construct achieved homogeneous, highly reliable co-expression of actuator and reporter in cell bodies across layers 2/3 and 5, with very little expression in layer 4 (Fig. 2B). Using a 210  $\mu\text{s}$  spiral photostimulation protocol, we achieved kHz ensemble stimulation over 1 mm<sup>2</sup> of superficial layer 2/3 in V1, with comparable efficiency across the entire imaging field-of-view (Fig. 2, C and D, and fig. S4A). Sequential addressing of neuronal ensembles at 1 kHz resolution was readily feasible with high success rates (Fig. 2, E and F, and figs. S4, H to S, and

S5, I and J) and without apparent off-target modulation of neighboring neurons (Fig. 2G and figs. S5, K and L). This all-optical technology also allowed generation of 3D constellations of targets to simultaneously excite many neurons distributed across layer 2/3 and layer 5 (25, 26, 32) (Fig. 2, H and I, and fig. S4, B, C, and J). Thus, MultiSLM enabled high-speed read-write access to large groups of single neurons ( $N > 100$ ), distributed over millimeter spatial scales and multiple cortical layers.

### **Selective visual network recruitment by functional ensemble stimulation**

We used ChRmine and MultiSLM to selectively activate visually-tuned ensembles in V1 while recording from the surrounding neural population across layers 2/3 and 5 of cortex. Mice were head-fixed and ran on a floating ball (Fig. 3A). In this behaviorally naïve cohort ( $n=4$  mice), there was no task-specific training before sessions of combined visual stimulus presentation, in vivo imaging, and optogenetic stimulation.

Mice transduced in V1 with the opsin/GECI virus viewed drifting sine wave gratings (vertical,  $0^\circ$ , or horizontal,  $90^\circ$ , and varied contrast: 2, 12, 25, or 50%; Fig. 3B) while  $\text{Ca}^{2+}$  signals were recorded (Fig. 3, A to C, materials and methods). In each mouse, orientation-tuned ensembles were identified across layers ( $30 \pm 6.8$  neurons [mean $\pm$ SD]); two control ensembles were defined to match the number of cells in each orientation-tuned ensemble, but with member neurons randomly selected from the surrounding population (Fig. 3C; materials and methods). On randomly interleaved trials (Fig. 3D), either sine-wave gratings were presented, or one of the cellular ensembles was photostimulated (tuned- or random-ensemble with comparable photostimulation efficacy; fig. S10C; materials and methods). Visual stimulation was never paired with optogenetic stimulation within the same trials. Ensemble optogenetic stimulation drove time-locked responses matching temporal onset and offset of activity in the naturally-occurring (visual stimulus-evoked) ensembles (Fig. 3E); also observed was co-activation of non-stimulated neurons in the surrounding volume that were more likely to be similarly-tuned than orthogonally-tuned to the targeted ensemble (Fig. 3F, fig. S12A, left,  $p=0.025$ ,  $\chi^2$  two-tailed test,  $n=20$  sessions,  $n=4$  mice). This indicates that cortically-initiated activity in V1 defined by natural visually-evoked activity preferentially recruits the corresponding, broader visual-stimulus-tuned network.

To further examine the patterns of neural recruitment in the surrounding network following visual or optical stimulation, we developed a neural decoding approach involving both Principal Components Analysis (PCA) and binary classification (sparse logistic regression; Fig. 3G; materials and methods; figs. S10 and S11). From each experimental animal, we conservatively identified a subset of the held-out neurons,

termed “unstimulated neurons,” that had never been optogenetically stimulated under any experimental circumstances—and also were not within spatial proximity to any stimulated neuron (materials and methods; this exclusion protocol was also applied for Fig. 3F). This approach excluded many neurons ( $1885 \pm 232$  [mean $\pm$ SD] neurons, or  $46 \pm 4\%$  of all neurons in each dataset, from  $n=4$  mice; fig. S10A) but minimized any risk of including neurons directly stimulated only by virtue of proximity to optogenetic targets (figs. S5 and S6). We next examined

the single-trial activity in these unstimulated neurons in response to each visual stimulus. Only these visually-evoked data from the unstimulated neurons were used to identify Principal Component (PC) vectors and to separately train binary classifiers to predict stimulus ( $0^\circ/90^\circ$ ) from the unstimulated neurons. These visual-trained PCs and classifiers were then used to predict stimulus type for all experimental conditions (visual and tuned/random optogenetic).

The PCA results can be seen in Fig. 3H for two representative mice (analyzed independently; top and bottom row). Each single line in this panel represents the average 19-frame (6.92 s) trajectory traversed by the unstimulated neuron population during  $0^\circ$  (blue) and  $90^\circ$  (red) trial conditions on each experimental day. Following stimulus onset (denoted by bold red or blue dots), trajectories diverge as a function of visual stimulus type (left column). Neural trajectories were similar between visual stimulus and tuned-ensemble optogenetic stimulation conditions for both  $0^\circ$  (blue) and  $90^\circ$  (red) trial types (first two columns). In contrast, there was no apparent segregation of neural trajectories arising from random-ensemble stimulation (cells not selective for either the  $0^\circ$  or  $90^\circ$  visual stimulus; third column), nor in the absence of stimulation (fourth column). This segregation of trajectories among unstimulated-cell ensembles in different stimulus conditions was reproducible within individual mice and across mice: the top two principal components explained most of the variance ( $76.21 \pm 2.09\%$ ) in the visually-evoked data (fig. S10B; top four explained  $89.96 \pm 0.46\%$ ). Importantly, we do not attribute the different effects of random and tuned optogenetic stimulation to photoactivation efficacy; we found no significant difference between the potency of stimulation of random- vs. tuned-ensembles ( $p=0.48$ ,  $n=4$  mice, paired  $t$  test; fig. S10C; materials and methods).

The unstimulated neuron population activity thus encodes the stimulus similarly during tuned-ensemble stimulation and visual stimulation, but not random-ensemble stimulation. This finding was developed in more quantitative detail with binary classifiers. The classifiers were able to find a sparse set of weights for the unstimulated neurons to cleanly separate visual conditions ( $0^\circ/90^\circ$ ) (fig. S10, D to K). By subtracting the trial-averaged fluorescence responses of these neurons during the  $0^\circ$  visual conditions, from those

during the 90° visual conditions, we resolved distinct groups of cells that exhibited differential recruitment during each visual stimulus (Fig. 3I, left column). This pattern was largely reproduced with tuned optogenetic stimulation (Fig. 3I, second column) but not seen during either random-ensemble stimulation or unstimulated activity (Fig. 3I, third and fourth columns; fig. S11). Together, these results indicate that population responses among the unstimulated neurons following tuned-ensemble optogenetic stimulation resemble those observed during visual stimulation—but are distinct from those seen during random-ensemble optogenetic stimulation (Fig. 3J). By examining classifier prediction accuracy, we found no significant difference between random-ensemble stimulation and the unstimulated condition ( $p=0.46$ ,  $n=20$  total conditions of each type, pooled across 4 mice and 5 conditions/mouse; Wilcoxon signed-rank test; Fig. 3K), whereas data taken from tuned-ensemble stimulation conditions yielded predictions superior to those seen with random-ensemble stimulation ( $p<0.001$ ,  $n=20$  conditions of each type, Wilcoxon signed-rank test; Fig. 3K).

#### ***Recruiting specific percepts at cellular resolution: behavioral and physiological readouts***

We trained a separate cohort of mice ( $n=7$ ) to high performance on a Go/No-Go visual discrimination task (Fig. 4, A and B). Each mouse learned to reliably discriminate high-contrast (12-50%), but not low-contrast (2%), oriented visual stimuli (Fig. 4C). Neurons responding to either the Target (0°, Go) or Distractor (90°, No-Go) stimulus ( $OSI>0.5$ ) were identified in the context of our task using the same criteria as before. Consistent with an increase in size, tuning sharpness and/or reliability of the population representation (33, 34), this identical procedure resulted in slightly more neurons in each ensemble compared to the untrained cohort ( $39.9 \pm 8.5$  [mean $\pm$ SD] vs.  $30 \pm 6.8$  neurons per trained mouse ensemble, respectively,  $p < 0.05$  two-tailed  $t$  test).

Two random ensembles (matched in size to the Go and No-Go ensembles, respectively) were defined with the same criteria as for the naïve cohort. We used the same ensembles on each subsequent day of the experiment, for each mouse. In each session, 75% of trials were high-contrast visual stimuli (1/3 as visual-only and 2/3 as visual-with-optogenetic stimulus) to promote task engagement and prevent extinction of the behavioral task. Of the remaining trials, either no stimulus was presented, or a tuned or random ensemble was optogenetically stimulated as the sole stimulus (Fig. 4, D to F). On the optogenetic-stimulation-only trials, mice were rewarded or punished in identical manner to visual-only trials. In this way, licking behavior during tuned- or random-ensemble stimulation was consistently rewarded or punished according to each ensemble's associated visual percept.

One of seven mice (mouse 3) correctly discriminated the

two tuned-ensemble optogenetic stimuli (without any visual stimulation) in the course of the first session ( $p<0.05$ , two-tailed Fisher's exact test, hit rate vs. false alarm rate,  $n=22$  trials,  $d'=2.2$ ). For the remaining animals, we gradually increased the visual contrast of the paired visual/optogenetic condition from 2% to 5% contrast over the course of several sessions. In these mice, concomitant optogenetic stimulation of orientation-specific ensembles succeeded in improving behavioral discrimination across the contrast ramp, including at the perceptual threshold of the animals (Fig. 4G,  $p<0.05$ , two-way ANOVA, main effect of optogenetic stimulation type,  $p<0.01$  tuned ensemble stimulation with visual vs. visual only Tukey HSD post hoc test,  $n=6/6$  mice that proceeded through the contrast ramp). After the conclusion of this contrast ramp, mice achieved high performance discrimination of tuned-ensemble optogenetic stimulation alone (i.e., with no visual stimulation;  $p<0.0001$ ,  $n=6$  mice, before vs. after contrast ramp; and tuned ensemble after ramp vs. no optogenetic stimulation,  $p<0.0001$  overall effect across stimulation conditions in Fig. 4H, ANOVA with Tukey HSD post hoc tests;  $6/6$  mice each significantly discriminated the tuned ensembles to at least  $p<0.05$  two-tailed Fisher's exact test within the first two sessions;  $4/6$  were significant  $p<0.01$  on the first day following the ramp). Tuned ensemble discrimination behavior was stable on the second day following the contrast ramp ( $p<0.0001$ ,  $n=5$  mice, including the third mouse 3 session, day 2 vs. no optogenetic stimulation and vs. after, ANOVA with Tukey HSD post hoc tests).

The observed high-performance discrimination of optogenetic ensembles defined based on visual response properties raises the question of whether discrimination performance might generalize upon stimulation of other, similarly defined, ensembles. To test this, we sampled a unique V1 population (changing the origin of our  $z$  axis by  $\Delta z=30\mu\text{m}$ ) and identified new populations of tuned-ensemble cells (defined according their 0°/90° responses, exactly following the original criteria). These new ensembles had never been directly optogenetically stimulated in previous experiments, but did share the same visual-tuning characteristics of the original ensembles. We designated new sets of random ensembles to match these new tuned ensembles and advanced immediately to the ensemble and/or high contrast visual discrimination task without an additional contrast ramp. All mice that progressed through to this new protocol ( $n=3$ ) were able to correctly abstract the tuned-ensemble optogenetic stimulus and discriminate these new ensembles ( $p<0.0001$  Fisher's exact tests,  $n=1-2$  sessions). We repeated our new ensembles experiment in an additional mouse with one specific change to the experimental protocol: never pairing the optogenetic activation of the new tuned or random ensembles with visual stimuli on any trial. Our results when removing this pairing with any visual conditions yielded similar results to those seen in the



other mice ( $p < 0.05$  Fisher's exact test,  $n = 28$  trials from  $n = 2$  sessions). Overall, mice could generalize tuned ensemble stimulation discrimination behavior with high performance (Fig. 4H,  $p < 0.0001$  new ensemble vs. no stimulation,  $p > 0.99$  day 2 and after vs. new ensembles, ANOVA with Tukey HSD post hoc tests).

Results were more variable for random-ensemble stimulation across mice, with only one of six mice significantly discriminating random ensembles immediately following the contrast ramp ( $p < 0.0001$  Fisher's exact test;  $p = 0.14$  after vs. no stimulation,  $p = 0.37$  after vs. before,  $n = 6$  mice,  $p < 0.01$  main effect of optogenetic stimulation type across all conditions in Fig. 4I, ANOVA with Tukey HSD post hoc tests; mouse 3 could discriminate random ensembles over the course of his second session,  $p < 0.0001$  Fisher's exact test,  $n = 22$  trials). Tuned-ensemble stimulation drove higher performance across mice than did the random-ensemble stimulation ( $p < 0.01$ , two-tailed paired  $t$  test,  $n = 7$  mice). This result might be partly explained by the relative efficacy of random stimulation: we found that, in contrast to the naïve cohort, here a higher fraction of neurons within tuned-ensembles were confirmed to be activated by optogenetic stimulation than with random-ensembles (fig. S12D,  $p < 0.001$ , paired  $t$  test,  $n = 3$  mice, materials and methods). On the next session (or the third mouse 3 session), the population effect for random ensemble discrimination was significant compared to no stimulation and after the contrast ramp, driven by the subset of mice that had learned the discrimination (Fig. 4I,  $p < 0.01$  and  $p < 0.05$  respectively,  $n = 7$  mice, ANOVA with Tukey HSD post hoc test; a third mouse out of seven eventually learned to discriminate the random ensembles;  $p < 0.001$  Fisher's exact test data from  $n = 5$  sessions). Unlike behavior for new tuned ensembles (Fig. 4H, above), mice could not generalize their discrimination performance from the trained random ensembles to new random ensembles within the same sessions (Fig. 4I,  $p < 0.05$  day 2 vs. new ensembles and  $p < 0.01$  day 2 stimulation vs. no stimulation,  $p = 0.97$  new ensembles vs. no stimulation, ANOVA with Tukey HSD post hoc tests,  $n = 4$  mice, including 2/3 mice that learned to discriminate the first random ensembles; new-random-ensemble trials interleaved with new-tuned-ensemble trials in same sessions).

Five of the seven mice advanced to additional experiments (see below) and were used for all neural analyses. We asked what effects the pairing of visual stimuli with optogenetic ensemble-stimulation might have on specific visual circuit dynamics (Fig. 4, J to N). To perform this analysis we examined neurons for each experiment day that were never stimulated (and thus were not part of the original tuned ensemble from day 1), but responded selectively to one of the two visual stimuli ( $OSI > 0.5$ ) on that day, and also responded reliably during ensemble-only stimulation (Wilcoxon signed-rank test

comparing baseline and sample window periods, materials and methods). This defined “iso-tuned” and “ortho-tuned” co-active populations based on the relative tuning (or designated for  $0^\circ$  or  $90^\circ$  for the random ensembles) of the stimulated ensemble. All of these local network recruitment analyses used only data from each trial after stimulus onset, but before any reward or punishment was delivered (materials and methods). Whereas selective recruitment of iso-tuned populations was observed for tuned-ensemble stimulation before the contrast ramp in trained mice (Fig. 4J,  $p < 0.05$ ,  $\chi^2$  two-tailed test,  $n = 6$  sessions in 5 mice), as in naïve mice (fig. S12A), random-ensemble stimulation did not recruit visual-percept specific populations (Fig. 4K,  $p = 0.87$ ,  $\chi^2$  two-tailed test,  $n = 6$  sessions in 5 mice). Comparing recruitment of tuned networks in our trained vs. naïve cohorts, we observed that learning the visual task alone enhanced specific network recruitment in response to visual stimuli (fig. S12A, right,  $p < 0.05$ ;  $\chi^2$  two-tailed test,  $n = 20$  sessions in 4 mice). Following the contrast ramp experiments, tuned ensemble stimulation much more powerfully recruited the iso-tuned population (Fig. 4L;  $p < 0.0001$ ,  $\chi^2$  two-tailed test: iso-tuned vs. orthogonally tuned,  $n = 15$  sessions in 5 mice;  $p < 0.0001$ ,  $\chi^2$  two-tailed test before vs. after the contrast ramp, same sessions as random-ensemble stimulation). Similarly, random-ensemble stimulation following the ramp training preferentially recruited the iso-tuned populations that they were paired with during the ramp (Fig. 4M,  $p < 0.0001$ ,  $\chi^2$  two-tailed test vs. orthogonally-tuned). The magnitude of iso-tuned population recruitment also increased after vs. before contrast ramp experiments (Fig. 4N,  $p < 0.0001$ ,  $\chi^2$  two-tailed test), consistent with the newly-learned ability of specific mice to perform random-ensemble discrimination (e.g., mouse 5, orange points in Fig. 4, M and N, was the best performer in Fig. 4I after ramp). Still, tuned-ensembles were much more effective at recruiting iso-tuned populations than random-ensembles (Fig. 4N,  $p < 0.0001$ ,  $\chi^2$  two-tailed test).

We explored the stability of visual-percept specific networks and optogenetic-percept discrimination behavior following the contrast ramp in these same five mice (Fig. 5 and figs. S12 to S14). Mice continued to perform both visual and optogenetic-percept discrimination behaviors with high performance over the course of many weeks (Fig. 5A, 109/112 visual and 107/112 tuned-ensemble sessions with  $p < 0.05$  hit rate vs. false alarm rate, two-tailed Fisher's exact tests). Behavioral performance was nearly identical for discriminating visual orientations and optogenetic ensembles (Fig. 5B,  $91.12 \pm 0.75\%$  correct vs.  $89.47 \pm 0.78\%$  correct [mean  $\pm$  SEM] respectively,  $p = 0.13$ , two-tailed paired  $t$  test,  $n = 112$  sessions across 5 mice).

### ***Both naturally and optogenetically recruited ensembles support behavior***

Analyzing all sessions post-contrast ramp, we measured recruitment of iso-tuned and orthogonally-tuned neurons and identified co-active neurons among the unstimulated population during optogenetic-only stimulus (Fig. 5C). Iso-tuned neurons were much more likely to be recruited than orthogonally-tuned neurons (Fig. 5D,  $p < 0.0001$ ,  $\chi^2$  two-tailed test, data from  $n=58$  sessions in 5 mice). Iso-tuned population recruitment also increased with the number of neurons stimulated (Fig. 5E; Spearman's  $\rho=0.34$ ,  $p < 0.001$ ,  $n=116$  data points across 5 mice). Recruitment of orthogonally tuned neurons, however, decreased in probability as the number of stimulated neurons increased (Fig. 5E; Spearman's  $\rho=-0.24$ ,  $p < 0.01$ ,  $n=116$  data points across 5 mice). Thus, selective recruitment was generally much more robust than orthogonal recruitment across all conditions tested (Fig. 5E;  $p < 0.0001$ , Fisher's z transformation).

We further analyzed the activity evoked in unstimulated neurons (materials and methods; fig. S12B; see Fig. 3G). As with the naïve cohort, we identified PC vectors using data taken during the visual-only stimuli and used these PC dimensions to project all of the experimental condition types (Fig. 5F). The first two principal components explained the majority of the variance ( $67.97 \pm 4.56\%$ , mean  $\pm$  s.e.m.; fig. S12C). Neural trajectories during both visual and tuned-optogenetic stimulation closely matched each other, with the Target and Distractor trajectories separating upon stimulation onset (dark blue or red dot, imaging frame following stimulus onset), and exhibited far less separation during random-ensemble stimulation (e.g., no separation detectable in mouse 1; Fig. 5F, top row, third column), and only slight separation in mouse 3 (Fig. 5F; bottom row/third column)—a mouse that notably learned to reliably discriminate random ensembles.

The principal components that we used to plot our neural trajectories appear to primarily describe visual information, rather than behavioral state. This is a critical distinction because behavioral task engagement can modulate activity in V1 (35–37), potentially confounding our interpretation. However, we note that the neural trajectories from sessions where the mouse performed the incorrect licking behavior more than 50% of the time were indistinguishable from trajectories in sessions with high performance (see Fig. 5F, left two columns, dark blue and red lines correspond to these low performance conditions). This result revealed the independence of the V1 trajectories from strictly motor- or action decision-related effects and supports the interpretation that they represent sensory/perceptual information.

A binary classifier was trained on unstimulated neuron data taken from two frames following visual stimulus onset, but prior to reward (fig. S12, E to N). The learned classifier weights corresponded to neurons with selective responses for

the  $0^\circ$  or  $90^\circ$  visual stimuli. Crucially, these same neurons were selectively recruited by their corresponding optogenetic ensembles (Fig. 5G; three additional mice shown in fig. S13). This result is consistent with a model where the similarity of neural representations across visual-only and tuned-ensemble stimuli reveals the formation of a similar percept. The fact that the magnitude of the recruited population response is larger during tuned-optogenetic versus visual stimulation is consistent with behavioral training enhancing network recruitment of iso-tuned neurons, and may explain how random-ensemble stimulation could yield population responses that weakly discriminate condition type (Fig. 5, F to H, bottom row, third column in each of those three panels). In contrast, random-ensemble stimulation never evoked a large population response in naïve animals (Fig. 3, H to K, and fig. S11).

We identified a high correlation between mouse behavior and ensemble classifier performance across mice and condition type (Fig. 5I;  $r^2=0.66$ ,  $p < 0.0001$ ). Both classifier and behavioral data operated near saturation on real visual data, and on tuned-ensemble stimulation conditions. In contrast, random-ensemble stimulation resulted in lower neural and behavioral discrimination.

### ***Quantitative circuit architecture underlying layer-specific perceptual thresholds***

In a subset of trials, we stimulated subsets of neurons selected at random from the original tuned ensembles, recapitulating our discrimination experiments as a function of ensemble size and laminar position. Stimulating only layer 2/3 tuned-ensembles led to selective recruitment of iso-tuned neurons in both layer 2/3 and layer 5, with stronger recruitment occurring within layer 2/3 (Fig. 6A,  $p < 0.0001$  for all comparisons: recruited iso-tuned vs. ortho-tuned, and within layer 2/3 vs. layer 5,  $\chi^2$  two-tailed tests). Increasing the number of neurons stimulated in layer 2/3 led to an increase in the fraction of co-active iso-tuned cells within both layer 2/3 and layer 5 (Fig. 6B, Spearman's  $\rho=0.46$ ,  $p < 0.01$ ,  $n=46$  data points, within layer 2/3,  $\rho=0.51$ ,  $p < 0.01$ ,  $n=36$  data points, within layer 5,  $p=0.78$  two-tailed Fisher's z transformation comparing  $\rho$  values).

In contrast, stimulating only layer 5 tuned-ensembles led to selective recruitment within layer 5, but did not lead to robust recruitment in layer 2/3. Layer 5 to layer 2/3 recruitment was not visual-percept selective (Fig. 6C,  $p < 0.0001$ , iso vs. ortho tuned in layer 5, and layer 5 vs. layer 2/3 iso tuned,  $\chi^2$  two tailed tests; recruitment in layer 2/3 was not significantly different between iso and ortho tuned populations,  $p=0.58$ ,  $\chi^2$  two-tailed test). As the number of neurons stimulated increased in layer 5, a greater fraction of iso-tuned neurons in the surrounding population was recruited in layer 5 but not layer 2/3 (Fig. 6D, Spearman's  $\rho=0.62$ ,  $p < 0.01$ ,  $n=24$

data points for layer 5 recruitment;  $\rho=0.19$ ,  $p=0.38$ ,  $n=24$  data points for layer 2/3 recruitment), and the correlation was stronger for layer 5 than even the weak positive trend for layer 2/3 (Fig. 6D,  $p<0.05$ , Fisher's  $z$  transformation).

Stimulating the original tuned-ensembles across layers led to selective recruitment within both layer 2/3 and layer 5, with the strongest iso-tuned recruitment in layer 5 (fig. S15A,  $p<0.0001$  all comparisons shown between iso vs. ortho-tuned and layer 2/3 vs. layer 5,  $\chi^2$  two tailed tests). Furthermore, increasing the number of stimulated layer 5 neurons more rapidly recruited higher proportions of iso-tuned layer 5 neurons than did stimulating layer 2/3 neurons recruited iso-tuned layer 2/3 cells (fig. S15B,  $p<0.01$ , ANCOVA, controlling for the covariate of number stimulated).

These layer-specific results indicate selective functional connectivity within layer 2/3, to a greater extent within layer 5, and from layer 2/3 to layer 5. Strong functional connectivity is markedly lacking from layer 5 to layer 2/3, and functional effects of that projection appear non-specific in terms of the visual-percept information investigated here. Over all layer-specific and full, original ensemble stimulation conditions, we found a strong, rapid increase in the fraction of recruited iso-tuned neurons across the cortical volume as the number of stimulated neurons increased (fig. S16, Spearman's  $\rho=0.71$ ,  $p<0.0001$ ,  $n=186$  data points; combining data shown in Fig. 5E and full volume, across layers recruitment data corresponding to the experiments shown in Fig. 6, A to D).

We next examined the relationship between the size and laminar location of the tuned-ensemble stimulus, and its consequences on both the recruited population and behavior. Using the binary classifiers operating on unstimulated cells revealed that, across subjects, there was a critical number of stimulated neurons required for recruiting a robust population response, driving high discrimination performance (Fig. 6, E and F; for psychometric curve fitting, see materials and methods and fig. S15, C to G). Once  $\sim 20$  iso-tuned neurons were stimulated, we found that classifier performance saturated at nearly 100%—indicating that ensembles of this order drive specific network dynamics that are above a threshold necessary for high-performance discrimination. Importantly, we found similar results when analyzing aggregate behavioral performance (Fig. 6, G and H). Together, these results suggest that beyond this threshold of activity in only a few tens of neurons, network amplification mechanisms reliably carry signals outside of V1 to drive specific behavior.

Comparison of the psychometric curves suggested that layer 5 neurons may be more potent at driving neural discrimination than those in layer 2/3. We therefore restricted our analysis to experiments with comparable tuned-ensemble sizes, comparing the effect of laminar position on the ability to influence classifier performance (Fig. 6F) or animal

behavior (Fig. 6H). In each case, equivalent numbers of layer 5 neurons were more successful at driving high performance ( $F_{1,49}=8.11$ ,  $p<0.01$  for the classifier data;  $F_{1,49}=5.47$ ,  $p=0.023$  for behavioral data, main effect of layer). To assess the minimum ensemble size for discrimination, we carried out further experiments in the most sensitive two mice. Both mice could discriminate two neurons per ensemble in layer 5 with high performance ( $p=0.037$  and  $p=0.036$ , two-tailed Fisher's exact test,  $n=24$ , and  $n=23$  trials for each mouse, respectively). We did not find significant behavioral discrimination results stimulating single neurons in any mice.

## Discussion

We found that when small subsets of visual stimulus-specific tuned ensembles were sufficiently activated in mouse V1, selective but widespread activation was observed across the broader network and concomitant behavioral performance resulted. The specific recruitment of tuned ensembles was seen in naïve mice but increased with learning of a visual task and was further heightened by optogenetic drive of percept-selective tuned subsets during discrimination behavior. Optogenetic stimulation of tuned-ensembles in layer 5 was more potent than layer 2/3 at eliciting percept-selective network recruitment as well as the correct behavior, with interlaminar recruitment favored from superficial to deep layers. With repeated optogenetic excitation of random-ensembles during behavioral training with paired visual stimuli, non-tuned cells could become linked into the visual percept-specific ensembles. These random-ensembles could subsequently drive the corresponding behavior, consistent with candidate Hebbian mechanisms for circuit plasticity underlying learning (19, 20, 38, 39). Behavioral and neural decoding results (in both trained and naïve mice) suggested the optogenetic excitation of each tuned-ensemble ( $0^\circ/90^\circ$ ) triggered a percept closer to their corresponding visual stimulus than the opposing one. This was supported by our finding that mice could generalize and immediately discriminate optogenetic excitation of held-out, visual-percept-selective ensembles, and behave correctly.

The volumetric all-optical approach employed here revealed numerous cortical functional-architecture insights relating to visual perception in the behaving mammal. Monosynaptic/reciprocally-connected subnetworks of similarly-tuned neurons in layer 2/3 of mouse V1 have been recently reported, using *ex vivo* paired recording and electron-microscopy connectomic studies of nearby cells (7, 9–11). The specific recruitment that we observe within layer 2/3 *in vivo* may depend upon this wiring architecture. A recent study of the relationship between orientation tuning and monosynaptic input to layer 2/3 V1 neurons (8, 40) also found that layer 2/3 inputs to a layer 2/3 pyramidal cell tend to be similarly tuned with the post-synaptic cell. Conversely, inputs from



layer 5 to the layer 2/3 cell were more likely, on average, to prefer a different orientation than the post-synaptic neuron [also see ref. (41)]—consistent with our findings that layer 5 to layer 2/3 recruitment was not tuning-specific. The more robust tuned ensemble recruitment of layer 5 versus layer 2/3 that we observed may expose a circuit for recruiting cortico-cortical and corticostriatal output neurons (42, 43) key for behavior, perhaps leveraging high reciprocal connectivity of striatum-projecting layer 5 neurons that has been observed in other sensory cortical areas (44).

Stimulation of a critical number of selectively-tuned V1 neurons both recruited a substantial fraction of the iso-tuned ensemble and supported high performance behavioral discrimination. To further explore features of V1 architecture that could permit critically excitable network recruitment and avoid frequent spontaneous widespread excitation (i.e., false percepts resulting from spontaneous activity), we developed an analytic theory (see supplementary text). In this context, we first estimated the minimum number of stimulated neurons that could trigger widespread dynamics like those found here to be associated with a percept under biologically plausible assumptions about the total size of individual sub-networks that share common orientation tunings, spontaneous firing rates, and single neuron integration times. This theoretical lower limit for this threshold revealed that V1 circuitry may operate in a regime consistent with our experiments that is as sensitive as possible to external stimulation, while still avoiding spontaneously driven false positive percepts. To provide proof-of-principle support for this theory, we constructed a network model (see supplementary text, fig. S17) for an iso-tuned ensemble of  $N$  excitatory and inhibitory neurons, whose connectivity could be critically tuned to achieve both high sensitivity to external inputs, with external stimulation of only  $O(\sqrt{N})$  neurons required to yield a response in  $O(N)$  neurons, yet still admit a stable state of low spontaneous activity. Thus, our theory builds upon our experimental findings to reveal that V1 might operate in a critically excitable dynamic regime that simultaneously enables highly sensitive amplification of external stimulation, low spontaneous activity rates, and low excitation thresholds for reliably triggering percepts.

Based on our experimental results, optogenetically-evoked percepts likely resembled corresponding visual percepts sufficiently to recruit the corresponding naturalistic visual-like neural dynamics and support robust and generalizable discrimination behavior. Nevertheless, mice initially required some training involving paired optogenetic and visual stimuli before optogenetic activation alone sufficed to drive behavioral discrimination. Full natural visual percepts (especially beyond responses to simple drifting grating stimuli) may require activation of diverse cortical and subcortical

brain areas (45–47), with patterns that span greater retinotopic, functional and/or temporal dimensions than explored here. Understanding which patterns of V1 stimulation recruit higher visual areas (48–52) and reverberating activation of parietal and prefrontal cortical areas, as hypothesized for visual perception (1–3), is also a necessary next step. Our results also revealed an intricate link between plasticity and performance on a learned perceptually-guided task, building upon intrinsic features of V1 seen in behaviorally naïve mice. Future studies are thus needed to further explore the broad space of possible spatiotemporal parameters that can be used to write in single-neuron activity, and of behavioral paradigms that can be designed to further study perceptual and learning-related mechanisms. These outcomes will permit detailed studies of the plasticity mechanisms underlying learning—and of the elements of neural activity that are required to drive specific perceptual experiences.

The MultiSLM approach readily allows expanding the addressable field of view in tandem with wide-field mesoscopic imaging methods [e.g., via spatial tiling; see supplementary text and figs. S18 and S19; (53)]. Such investigation of broader networks over multiple areas will be further enabled by the sensitivity and potency of ChRmine in allowing safe and effective optical recruitment of large ensembles of individually-defined cells. Improvements in temporal resolution and signal-to-noise of next-generation optical sensors may help further advance precise emulation of observed large-scale network activity, leveraging the kilohertz and millisecond resolution of MultiSLM and ChRmine optogenetic stimulation. Integration with advanced, deep cellular-resolution readouts such as GRIN lenses and Neuropixels electrodes (54, 55) may also enable assessment of relevant subcortical circuits. Importantly, these findings (54, 55) as well as the present study reveal that properly targeted optogenetics recruits naturalistic cell ensembles and brain dynamics—whether at the level of local microcircuits (54 and present study), regional circuits (present study), or global brainwide dynamics (55).

Studying specific sensory experiences with ensemble stimulation under different conditions may help advance development of therapeutic strategies, for neural prosthetics (56, 57) as well as for neuropsychiatric symptoms such as those involving hallucinations or delusions. More broadly, the ability to track and control large cellular-resolution ensembles over time during learning, and to selectively link new cells and ensembles together into behaviorally relevant circuitry, may have important implications for studying and leveraging plasticity underlying learning and memory in health and disease.



## Methods summary

All animal procedures followed animal care guidelines approved by Stanford University's Administrative Panel on Laboratory Animal Care (APLAC) and guidelines of the National Institutes of Health. ChRmine was discovered and then characterized using structure-guided genome mining followed by single- and multi-photon electrophysiology experiments. Mice were injected with a single bicistronic virus encoding both ChRmine and the  $\text{Ca}^{2+}$  indicator GCaMP6m. The Multi-SLM microscope was used to read and write neural activity throughout a volume of visual cortex. Both naïve mice, and mice trained on a go/no-go visual discrimination task, were habituated on the MultiSLM.  $\text{Ca}^{2+}$  imaging data obtained using the MultiSLM were analyzed to identify neurons tuned to visual cues. Mice performed the discrimination task with visual-only cues and/or optogenetic stimulation of the tuned ensembles. Unstimulated neurons from the  $\text{Ca}^{2+}$  imaging data were processed for neural circuit recruitment analyses. Detailed procedures for the experiments and data analyses are described in the supplementary materials.

## REFERENCES AND NOTES

1. B. van Vugt, B. Dagnino, D. Vartak, H. Safaai, S. Panzeri, S. Dehaene, P. R. Roelfsema, The threshold for conscious report: Signal loss and response bias in visual and frontal cortex. *Science* **360**, 537–542 (2018). [doi:10.1126/science.aar7186](https://doi.org/10.1126/science.aar7186) Medline
2. M. R. Joglekar, J. F. Mejias, G. R. Yang, X.-J. Wang, Inter-areal balanced amplification enhances signal propagation in a large-scale circuit model of the primate cortex. *Neuron* **98**, 222–234.e8 (2018). [doi:10.1016/j.neuron.2018.02.031](https://doi.org/10.1016/j.neuron.2018.02.031) Medline
3. S. Dehaene, J.-P. Changeux, Experimental and theoretical approaches to conscious processing. *Neuron* **70**, 200–227 (2011). [doi:10.1016/j.neuron.2011.03.018](https://doi.org/10.1016/j.neuron.2011.03.018) Medline
4. G. A. Mashour, The controversial correlates of consciousness. *Science* **360**, 493–494 (2018). [doi:10.1126/science.aat5616](https://doi.org/10.1126/science.aat5616) Medline
5. D. K. Murphey, J. H. R. Maunsell, M. S. Beauchamp, D. Yoshor, Perceiving electrical stimulation of identified human visual areas. *Proc. Natl. Acad. Sci. U.S.A.* **106**, 5389–5393 (2009). [doi:10.1073/pnas.0804998106](https://doi.org/10.1073/pnas.0804998106) Medline
6. C. D. Salzman, K. H. Britten, W. T. Newsome, Cortical microstimulation influences perceptual judgements of motion direction. *Nature* **346**, 174–177 (1990). [doi:10.1038/346174a0](https://doi.org/10.1038/346174a0) Medline
7. H. Ko, S. B. Hofer, B. Pichler, K. A. Buchanan, P. J. Sjöström, T. D. Mrsic-Flogel, Functional specificity of local synaptic connections in neocortical networks. *Nature* **473**, 87–91 (2011). [doi:10.1038/nature09880](https://doi.org/10.1038/nature09880) Medline
8. A. Wertz, S. Trenholm, K. Yonehara, D. Hillier, Z. Raics, M. Leinweber, G. Szalay, A. Ghanem, G. Keller, B. Rózsa, K.-K. Conzelmann, B. Roska, Single-cell-initiated monosynaptic tracing reveals layer-specific cortical network modules. *Science* **349**, 70–74 (2015). [doi:10.1126/science.aab1687](https://doi.org/10.1126/science.aab1687) Medline
9. L. Cossell, M. F. Iacuruso, D. R. Muir, R. Houlton, E. N. Sader, H. Ko, S. B. Hofer, T. D. Mrsic-Flogel, Functional organization of excitatory synaptic strength in primary visual cortex. *Nature* **518**, 399–403 (2015). [doi:10.1038/nature14182](https://doi.org/10.1038/nature14182) Medline
10. H. Ko, L. Cossell, C. Baragli, J. Antolik, C. Clopath, S. B. Hofer, T. D. Mrsic-Flogel, The emergence of functional microcircuits in visual cortex. *Nature* **496**, 96–100 (2013). [doi:10.1038/nature12015](https://doi.org/10.1038/nature12015) Medline
11. W.-C. A. Lee, V. Bonin, M. Reed, B. J. Graham, G. Hood, K. Glattfelder, R. C. Reid, Anatomy and function of an excitatory network in the visual cortex. *Nature* **532**, 370–374 (2016). [doi:10.1038/nature17192](https://doi.org/10.1038/nature17192) Medline
12. L. L. Glickfeld, M. L. Andermann, V. Bonin, R. C. Reid, Cortico-cortical projections in mouse visual cortex are functionally target specific. *Nat. Neurosci.* **16**, 219–226 (2013). [doi:10.1038/nn.3300](https://doi.org/10.1038/nn.3300) Medline
13. C. Y. L. Huh, J. P. Peach, C. Bennett, R. M. Vega, S. Hestrin, Feature-specific organization of feedback pathways in mouse visual cortex. *Curr. Biol.* **28**, 114–120.e5 (2018). [doi:10.1016/j.cub.2017.11.056](https://doi.org/10.1016/j.cub.2017.11.056) Medline
14. S. N. Chettih, C. D. Harvey, Single-neuron perturbations reveal feature-specific competition in V1. *Nature* **567**, 334–340 (2019). [doi:10.1038/s41586-019-0997-6](https://doi.org/10.1038/s41586-019-0997-6) Medline
15. R. J. Douglas, C. Koch, M. Mahowald, K. A. Martin, H. H. Suarez, Recurrent excitation in neocortical circuits. *Science* **269**, 981–985 (1995). [doi:10.1126/science.7638624](https://doi.org/10.1126/science.7638624) Medline
16. A. D. Lien, M. Scanziani, Tuned thalamic excitation is amplified by visual cortical circuits. *Nat. Neurosci.* **16**, 1315–1323 (2013). [doi:10.1038/nn.3488](https://doi.org/10.1038/nn.3488) Medline
17. K. D. Harris, T. D. Mrsic-Flogel, Cortical connectivity and sensory coding. *Nature* **503**, 51–58 (2013). [doi:10.1038/nature12654](https://doi.org/10.1038/nature12654) Medline
18. B. K. Murphy, K. D. Miller, Balanced amplification: A new mechanism of selective amplification of neural activity patterns. *Neuron* **61**, 635–648 (2009). [doi:10.1016/j.neuron.2009.02.005](https://doi.org/10.1016/j.neuron.2009.02.005) Medline
19. D. O. Hebb, *Organization of Behavior* (Wiley, 1949).
20. C. Clopath, L. Büsing, E. Vasilaki, W. Gerstner, Connectivity reflects coding: A model of voltage-based STDP with homeostasis. *Nat. Neurosci.* **13**, 344–352 (2010). [doi:10.1038/nn.2479](https://doi.org/10.1038/nn.2479) Medline
21. L. Carrillo-Reid, W. Yang, Y. Bando, D. S. Peterka, R. Yuste, Imprinting and recalling cortical ensembles. *Science* **353**, 691–694 (2016). [doi:10.1126/science.aaf7560](https://doi.org/10.1126/science.aaf7560) Medline
22. R. Prakash, O. Yizhar, B. Grewe, C. Ramakrishnan, N. Wang, I. Goshen, A. M. Packer, D. S. Peterka, R. Yuste, M. J. Schnitzer, K. Deisseroth, Two-photon optogenetic toolbox for fast inhibition, excitation and bistable modulation. *Nat. Methods* **9**, 1171–1179 (2012). [doi:10.1038/nmeth.2215](https://doi.org/10.1038/nmeth.2215) Medline
23. J. P. Rickgauer, K. Deisseroth, D. W. Tank, Simultaneous cellular-resolution optical perturbation and imaging of place cell firing fields. *Nat. Neurosci.* **17**, 1816–1824 (2014). [doi:10.1038/nn.3866](https://doi.org/10.1038/nn.3866) Medline
24. A. M. Packer, L. E. Russell, H. W. P. Dalgleish, M. Häusser, Simultaneous all-optical manipulation and recording of neural circuit activity with cellular resolution in vivo. *Nat. Methods* **12**, 140–146 (2015). [doi:10.1038/nmeth.3217](https://doi.org/10.1038/nmeth.3217) Medline
25. W. Yang, L. Carrillo-Reid, Y. Bando, D. S. Peterka, R. Yuste, Simultaneous two-photon imaging and two-photon optogenetics of cortical circuits in three dimensions. *eLife* **7**, e32671 (2018). [doi:10.7554/eLife.32671](https://doi.org/10.7554/eLife.32671) Medline
26. A. R. Mardinly, I. A. Oldenburg, N. C. Pégard, S. Sridharan, E. H. Lyall, K. Chesnov, S. G. Brohawn, L. Waller, H. Adesnik, Precise multimodal optical control of neural ensemble activity. *Nat. Neurosci.* **21**, 881–893 (2018). [doi:10.1038/s41593-018-0139-8](https://doi.org/10.1038/s41593-018-0139-8) Medline
27. P. J. Keeling, F. Burki, H. M. Wilcox, B. Allam, E. E. Allen, L. A. Amaral-Zettler, E. V. Armbrust, J. M. Archibald, A. K. Bharti, C. J. Bell, B. Beszteri, K. D. Bidle, C. T. Cameron, L. Campbell, D. A. Caron, R. A. Cattolico, J. L. Collier, K. Coyne, S. K. Davy, P. Deschamps, S. T. Dyhrman, B. Edvardsen, R. D. Gates, C. J. Gobler, S. J. Greenwood, S. M. Guida, J. L. Jacobi, K. S. Jakobsen, E. R. James, B. Jenkins, U. John, M. D. Johnson, A. R. Juhl, A. Kamp, L. A. Katz, R. Kiene, A. Kudryavtsev, B. S. Leander, S. Lin, C. Lovejoy, D. Lynn, A. Marchetti, G. McManus, A. M. Nedelcu, S. Menden-Deuer, C. Miceli, T. Mock, M. Montresor, M. A. Moran, S. Murray, G. Nadathur, S. Nagai, P. B. Ngam, B. Palenik, J. Pawlowski, G. Petroni, G. Piganeau, M. C. Posewitz, K. Rengefors, G. Romano, M. E. Rumpho, T. Rynearson, K. B. Schilling, D. C. Schroeder, A. G. B. Simpson, C. H. Slamovits, D. R. Smith, G. J. Smith, S. R. Smith, H. M. Sosik, P. Stief, E. Theriot, S. N. Twary, P. E. Umale, D. Vault, B. Wawrik, G. L. Wheeler, W. H. Wilson, Y. Xu, A. Zingone, A. Z. Worden, The Marine Microbial Eukaryote Transcriptome Sequencing Project (MMETSP): Illuminating the functional diversity of eukaryotic life in the oceans through transcriptome sequencing. *PLOS Biol.* **12**, e1001889 (2014). [doi:10.1371/journal.pbio.1001889](https://doi.org/10.1371/journal.pbio.1001889) Medline
28. T.-W. Chen, T. J. Wardill, Y. Sun, S. R. Pulver, S. L. Renninger, A. Baohan, E. R. Schreiter, R. A. Kerr, M. B. Orger, V. Jayaraman, L. L. Looger, K. Svoboda, D. S. Kim, Ultrasensitive fluorescent proteins for imaging neuronal activity. *Nature* **499**, 295–300 (2013). [doi:10.1038/nature12354](https://doi.org/10.1038/nature12354) Medline
29. J. C. D. Kaufmann, B. S. Krause, C. Grimm, E. Ritter, P. Hegemann, F. J. Bartl, Proton transfer reactions in the red light-activatable channelrhodopsin variant ReaChR and their relevance for its function. *J. Biol. Chem.* **292**, 14205–14216 (2017). [doi:10.1074/jbc.M117.779629](https://doi.org/10.1074/jbc.M117.779629) Medline

30. D. Urmann, C. Lorenz, S. M. Linker, M. Braun, J. Wachtveitl, C. Bamann, Photochemical properties of the red-shifted channelrhodopsin Chrimson. *Photochem. Photobiol.* **93**, 782–795 (2017). [doi:10.1111/php.12741](https://doi.org/10.1111/php.12741) [Medline](#)
31. C. A. Baker, Y. M. Elyada, A. Parra, M. M. Bolton, Cellular resolution circuit mapping with temporal-focused excitation of soma-targeted channelrhodopsin. *eLife* **5**, e14193 (2016). [doi:10.7554/eLife.14193](https://doi.org/10.7554/eLife.14193) [Medline](#)
32. M. Dal Maschio, J. C. Donovan, T. O. Helmbrecht, H. Baier, Linking neurons to network function and behavior by two-photon holographic optogenetics and volumetric imaging. *Neuron* **94**, 774–789.e5 (2017). [doi:10.1016/j.neuron.2017.04.034](https://doi.org/10.1016/j.neuron.2017.04.034) [Medline](#)
33. J. Poort, A. G. Khan, M. Pachitariu, A. Nemri, I. Orsolic, J. Krupic, M. Bauza, M. Sahani, G. B. Keller, T. D. Mrsic-Flogel, S. B. Hofer, Learning enhances sensory and multiple non-sensory representations in primary visual cortex. *Neuron* **86**, 1478–1490 (2015). [doi:10.1016/j.neuron.2015.05.037](https://doi.org/10.1016/j.neuron.2015.05.037) [Medline](#)
34. A. Schoups, R. Vogels, N. Qian, G. Orban, Practising orientation identification improves orientation coding in V1 neurons. *Nature* **412**, 549–553 (2001). [doi:10.1038/35087601](https://doi.org/10.1038/35087601) [Medline](#)
35. Y. Fu, J. M. Tucciarone, J. S. Espinosa, N. Sheng, D. P. Darcy, R. A. Nicoll, Z. J. Huang, M. P. Stryker, A cortical circuit for gain control by behavioral state. *Cell* **156**, 1139–1152 (2014). [doi:10.1016/j.cell.2014.01.050](https://doi.org/10.1016/j.cell.2014.01.050) [Medline](#)
36. A. R. Seitz, D. Kim, T. Watanabe, Rewards evoke learning of unconsciously processed visual stimuli in adult humans. *Neuron* **61**, 700–707 (2009). [doi:10.1016/j.neuron.2009.01.016](https://doi.org/10.1016/j.neuron.2009.01.016) [Medline](#)
37. P. M. Goltstein, G. T. Meijer, C. M. Pennartz, Conditioning sharpens the spatial representation of rewarded stimuli in mouse primary visual cortex. *eLife* **7**, e37683 (2018). [doi:10.7554/eLife.37683](https://doi.org/10.7554/eLife.37683) [Medline](#)
38. E. L. Bienenstock, L. N. Cooper, P. W. Munro, Theory for the development of neuron selectivity: Orientation specificity and binocular interaction in visual cortex. *J. Neurosci.* **2**, 32–48 (1982). [doi:10.1523/JNEUROSCI.02-01-00032.1982](https://doi.org/10.1523/JNEUROSCI.02-01-00032.1982) [Medline](#)
39. H. Markram, W. Gerstner, P. J. Sjöström, A history of spike-timing-dependent plasticity. *Front. Synaptic Neurosci.* **3**, 4 (2011). [doi:10.3389/fnsyn.2011.00004](https://doi.org/10.3389/fnsyn.2011.00004) [Medline](#)
40. J. H. Marshel, T. Mori, K. J. Nielsen, E. M. Callaway, Targeting single neuronal networks for gene expression and cell labeling in vivo. *Neuron* **67**, 562–574 (2010). [doi:10.1016/j.neuron.2010.08.001](https://doi.org/10.1016/j.neuron.2010.08.001) [Medline](#)
41. Y. Yoshimura, J. L. M. Dantzker, E. M. Callaway, Excitatory cortical neurons form fine-scale functional networks. *Nature* **433**, 868–873 (2005). [doi:10.1038/nature03252](https://doi.org/10.1038/nature03252) [Medline](#)
42. E. J. Kim, A. L. Juavinett, E. M. Kyubwa, M. W. Jacobs, E. M. Callaway, Three types of cortical layer 5 neurons that differ in brain-wide connectivity and function. *Neuron* **88**, 1253–1267 (2015). [doi:10.1016/j.neuron.2015.11.002](https://doi.org/10.1016/j.neuron.2015.11.002) [Medline](#)
43. K. D. Harris, G. M. G. Shepherd, The neocortical circuit: Themes and variations. *Nat. Neurosci.* **18**, 170–181 (2015). [doi:10.1038/nn.3917](https://doi.org/10.1038/nn.3917) [Medline](#)
44. S. P. Brown, S. Hestrin, Intracortical circuits of pyramidal neurons reflect their long-range axonal targets. *Nature* **457**, 1133–1136 (2009). [doi:10.1038/nature07658](https://doi.org/10.1038/nature07658) [Medline](#)
45. M. Siegel, T. J. Buschman, E. K. Miller, Cortical information flow during flexible sensorimotor decisions. *Science* **348**, 1352–1355 (2015). [doi:10.1126/science.1250551](https://doi.org/10.1126/science.1250551) [Medline](#)
46. R. Romo, V. de Lafuente, Conversion of sensory signals into perceptual decisions. *Prog. Neurobiol.* **103**, 41–75 (2013). [doi:10.1016/j.pneurobio.2012.03.007](https://doi.org/10.1016/j.pneurobio.2012.03.007) [Medline](#)
47. C.-T. Law, J. I. Gold, Reinforcement learning can account for associative and perceptual learning on a visual-decision task. *Nat. Neurosci.* **12**, 655–663 (2009). [doi:10.1038/nn.2304](https://doi.org/10.1038/nn.2304) [Medline](#)
48. J. H. Marshel, M. E. Garret, I. Nauhaus, E. M. Callaway, Functional specialization of seven mouse visual cortical areas. *Neuron* **72**, 1040–1054 (2011). [doi:10.1016/j.neuron.2011.12.004](https://doi.org/10.1016/j.neuron.2011.12.004) [Medline](#)
49. M. L. Andermann, A. M. Kerlin, D. K. Roumis, L. L. Glickfeld, R. C. Reid, Functional specialization of mouse higher visual cortical areas. *Neuron* **72**, 1025–1039 (2011). [doi:10.1016/j.neuron.2011.11.013](https://doi.org/10.1016/j.neuron.2011.11.013) [Medline](#)
50. M. M. Roth, F. Helmchen, B. M. Kampa, Distinct functional properties of primary and posteromedial visual area of mouse neocortex. *J. Neurosci.* **32**, 9716–9726 (2012). [doi:10.1523/JNEUROSCI.0110-12.2012](https://doi.org/10.1523/JNEUROSCI.0110-12.2012) [Medline](#)
51. G. N. Pho, M. J. Goard, J. Woodson, B. Crawford, M. Sur, Task-dependent representations of stimulus and choice in mouse parietal cortex. *Nat. Commun.* **9**, 2596 (2018). [doi:10.1038/s41467-018-05012-y](https://doi.org/10.1038/s41467-018-05012-y) [Medline](#)
52. M. Carandini, A. K. Churchland, Probing perceptual decisions in rodents. *Nat. Neurosci.* **16**, 824–831 (2013). [doi:10.1038/nn.3410](https://doi.org/10.1038/nn.3410) [Medline](#)
53. S. J. Yang, W. E. Allen, I. Kauvar, A. S. Andalman, N. P. Young, C. K. Kim, J. H. Marshel, G. Wetzstein, K. Deisseroth, Extended field-of-view and increased-signal 3D holographic illumination with time-division multiplexing. *Opt. Express* **23**, 32573–32581 (2015). [doi:10.1364/OE.23.032573](https://doi.org/10.1364/OE.23.032573) [Medline](#)
54. W. E. Allen, M. Z. Chen, N. Pichamoorthy, R. H. Tien, M. Pachitariu, L. Luo, K. Deisseroth, Thirst regulates motivated behavior through modulation of brainwide neural population dynamics. *Science* **364**, eaav3932 (2019). [Medline](#)
55. J. H. Jennings, C. K. Kim, J. H. Marshel, M. Raffee, L. Ye, S. Quirin, S. Pak, C. Ramakrishnan, K. Deisseroth, Interacting neural ensembles in orbitofrontal cortex for social and feeding behaviour. *Nature* **565**, 645–649 (2019). [doi:10.1038/s41586-018-0866-8](https://doi.org/10.1038/s41586-018-0866-8) [Medline](#)
56. S. J. Bensmaia, L. E. Miller, Restoring sensorimotor function through intracortical interfaces: Progress and looming challenges. *Nat. Rev. Neurosci.* **15**, 313–325 (2014). [doi:10.1038/nrn3724](https://doi.org/10.1038/nrn3724) [Medline](#)
57. D. J. O'Shea, E. Trautmann, C. Chandrasekaran, S. Stavisky, J. C. Kao, M. Sahani, S. Ryu, K. Deisseroth, K. V. Shenoy, The need for calcium imaging in nonhuman primates: New motor neuroscience and brain-machine interfaces. *Exp. Neurol.* **287**, 437–451 (2017). [doi:10.1016/j.expneurol.2016.08.003](https://doi.org/10.1016/j.expneurol.2016.08.003) [Medline](#)
58. Y. S. Kim, H. E. Kato, K. Yamashita, S. Ito, K. Inoue, C. Ramakrishnan, L. E. Fenno, K. E. Evans, J. M. Paggi, R. O. Dror, H. Kandori, B. K. Kobilka, K. Deisseroth, Crystal structure of the natural anion-conducting channelrhodopsin GtACR1. *Nature* **561**, 343–348 (2018). [doi:10.1038/s41586-018-0511-6](https://doi.org/10.1038/s41586-018-0511-6) [Medline](#)
59. H. E. Kato, F. Zhang, O. Yizhar, C. Ramakrishnan, T. Nishizawa, K. Hirata, J. Ito, Y. Aita, T. Tsukazaki, S. Hayashi, P. Hegemann, A. D. Maturana, R. Ishitani, K. Deisseroth, O. Nureki, Crystal structure of the channelrhodopsin light-gated cation channel. *Nature* **482**, 369–374 (2012). [doi:10.1038/nature10870](https://doi.org/10.1038/nature10870) [Medline](#)
60. G. T. Prusky, R. M. Douglas, Characterization of mouse cortical spatial vision. *Vision Res.* **44**, 3411–3418 (2004). [doi:10.1016/j.visres.2004.09.001](https://doi.org/10.1016/j.visres.2004.09.001) [Medline](#)
61. A. Forli, D. Vecchia, N. Binini, F. Succol, S. Bovetti, C. Moretti, F. Nespoli, M. Mahn, C. A. Baker, M. M. Bolton, O. Yizhar, T. Fellin, Two-photon bidirectional control and imaging of neuronal excitability with high spatial resolution in vivo. *Cell Reports* **22**, 3087–3098 (2018). [doi:10.1016/j.celrep.2018.02.063](https://doi.org/10.1016/j.celrep.2018.02.063) [Medline](#)
62. G. Thalhammer, R. W. Bowman, G. D. Love, M. J. Padgett, M. Ritsch-Marte, Speeding up liquid crystal SLMs using overdrive with phase change reduction. *Opt. Express* **21**, 1779–1797 (2013). [doi:10.1364/OE.21.001779](https://doi.org/10.1364/OE.21.001779) [Medline](#)
63. E. Ronzitti, M. Guillon, V. de Sars, V. Emiliani, LCoS nematic SLM characterization and modeling for diffraction efficiency optimization, zero and ghost orders suppression. *Opt. Express* **20**, 17843–17855 (2012). [doi:10.1364/OE.20.017843](https://doi.org/10.1364/OE.20.017843) [Medline](#)
64. W. Yang, J. E. Miller, L. Carrillo-Reid, E. Pnevmatikakis, L. Paninski, R. Yuste, D. S. Peterka, Simultaneous multi-plane imaging of neural circuits. *Neuron* **89**, 269–284 (2016). [doi:10.1016/j.neuron.2015.12.012](https://doi.org/10.1016/j.neuron.2015.12.012) [Medline](#)
65. S. Quirin, D. S. Peterka, R. Yuste, Instantaneous three-dimensional sensing using spatial light modulator illumination with extended depth of field imaging. *Opt. Express* **21**, 16007–16021 (2013). [doi:10.1364/OE.21.016007](https://doi.org/10.1364/OE.21.016007) [Medline](#)
66. M. A. A. Neil, R. Juskaitis, M. J. Booth, T. Wilson, T. Tanaka, S. Kawata, Adaptive aberration correction in a two-photon microscope. *J. Microsc.* **200**, 105–108 (2000). [doi:10.1046/j.1365-2818.2000.00770.x](https://doi.org/10.1046/j.1365-2818.2000.00770.x) [Medline](#)
67. E. A. Pnevmatikakis, D. Soudry, Y. Gao, T. A. Machado, J. Merel, D. Pfau, T. Reardon, Y. Mu, C. Lacefield, W. Yang, M. Ahrens, R. Bruno, T. M. Jessell, D. S. Peterka, R. Yuste, L. Paninski, Simultaneous denoising, deconvolution, and demixing of calcium imaging data. *Neuron* **89**, 285–299 (2016). [doi:10.1016/j.neuron.2015.11.037](https://doi.org/10.1016/j.neuron.2015.11.037) [Medline](#)
68. H. H. Schütt, S. Harmeling, J. H. Macke, F. A. Wichmann, Painfree and accurate Bayesian estimation of psychometric functions for (potentially) overdispersed data. *Vision Res.* **122**, 105–123 (2016). [doi:10.1016/j.visres.2016.02.002](https://doi.org/10.1016/j.visres.2016.02.002) [Medline](#)
69. F. Perez, B. E. Granger, IPython: A system for interactive scientific computing. *Comput. Sci. Eng.* **9**, 21–29 (2007). [doi:10.1109/MCSE.2007.53](https://doi.org/10.1109/MCSE.2007.53)
70. E. A. Oliphant, *Guide to NumPy* (Trelgol Publishing, 2006).

71. J. D. Hunter, Matplotlib: A 2D graphics environment. *Comput. Sci. Eng.* **9**, 90–95 (2007). [doi:10.1109/MCSE.2007.55](https://doi.org/10.1109/MCSE.2007.55)
72. W. McKinney, in *Proceedings of the 9th Python in Science Conference* (2010), pp. 51–56.
73. F. Pedregosa, G. Varoquaux, A. Gramfort, V. Michel, B. Thirion, O. Grisel, M. Blondel, P. Prettenhofer, R. Weiss, V. Dubourg, J. Vanderplas, A. Passos, D. Cournapeau, M. Brucher, M. Perrot, É. Duchesnay, Scikit-learn: Machine learning in Python. *J. Mach. Learn. Res.* **12**, 2825–2830 (2011).
74. E. Jones, T. Oliphant, P. Peterson, others, *SciPy: Open source scientific tools for Python* (2001); [www.scipy.org/](http://www.scipy.org/).
75. S. Skipper, J. Perktold, in *Proceedings of the 9th Python in Science Conference* (2010), pp. 57–61.
76. H. E. Kato, Y. S. Kim, J. M. Paggi, K. E. Evans, W. E. Allen, C. Richardson, K. Inoue, S. Ito, C. Ramakrishnan, L. E. Fenno, K. Yamashita, D. Hilger, S. Y. Lee, A. Berndt, K. Shen, H. Kandori, R. O. Dror, B. K. Kobilka, K. Deisseroth, Structural mechanisms of selectivity and gating in anion channelrhodopsins. *Nature* **561**, 349–354 (2018). [doi:10.1038/s41586-018-0504-5](https://doi.org/10.1038/s41586-018-0504-5) [Medline](#)
77. W. Denk, J. H. Strickler, W. W. Webb, Two-photon laser scanning fluorescence microscopy. *Science* **248**, 73–76 (1990). [doi:10.1126/science.2321027](https://doi.org/10.1126/science.2321027) [Medline](#)
78. A. Cheng, J. T. Gonçalves, P. Golshani, K. Arisaka, C. Portera-Cailliau, Simultaneous two-photon calcium imaging at different depths with spatiotemporal multiplexing. *Nat. Methods* **8**, 139–142 (2011). [doi:10.1038/nmeth1552](https://doi.org/10.1038/nmeth1552) [Medline](#)
79. J. Kadmon, H. Sompolinsky, Transition to chaos in random neuronal networks. *Phys. Rev. X* **5**, 041030 (2015). [doi:10.1103/PhysRevX.5.041030](https://doi.org/10.1103/PhysRevX.5.041030)
80. Y. Song, F. DiMaio, R. Y.-R. Wang, D. Kim, C. Miles, T. Brunette, J. Thompson, D. Baker, High-resolution comparative modeling with RosettaCM. *Structure* **21**, 1735–1742 (2013). [doi:10.1016/j.str.2013.08.005](https://doi.org/10.1016/j.str.2013.08.005) [Medlines](#)
81. T. J. Dolinsky, J. E. Nielsen, J. A. McCammon, N. A. Baker, PDB2PQR: An automated pipeline for the setup of Poisson-Boltzmann electrostatics calculations. *Nucleic Acids Res.* **32**, W665–W667 (2004). [doi:10.1093/nar/gkh381](https://doi.org/10.1093/nar/gkh381) [Medline](#)
82. Z. Peng, Y. Liu, L. Yao, Z. Cao, Q. Mu, L. Hu, L. Xuan, Improvement of the switching frequency of a liquid-crystal spatial light modulator with optimal cell gap. *Opt. Lett.* **36**, 3608–3610 (2011). [doi:10.1364/OL.36.003608](https://doi.org/10.1364/OL.36.003608) [Medline](#)
83. J. Diels, W. Rudolf, *Ultrashort Laser Pulse Phenomena* (Academic Press, ed. 2, 2006).

## ACKNOWLEDGMENTS

We thank the Deisseroth laboratory for support, particularly to A. Crow, L. Fenno, J. Dou, C. Lee, I.P. Lee, C. Delacruz, S. Pak, J. Melander, N. Pichamoorthy, and S. Serati. We also acknowledge feedback from E. Trautman, D. O'Shea and K. Shenoy. **Funding:** K.D. is supported by the DARPA Neuro-FAST program, NIMH, NIDA, NSF, the Simons Foundation, the Wiegers Family Fund, the Nancy and James Grosfeld Foundation, the H.L. Snyder Medical Foundation, and the Samuel and Betsy Reeves Fund. S.G. was supported by the Burroughs-Wellcome, McKnight, Simons, and James S. McDonnell foundations. J.K. was supported by the Swartz Foundation. This work was also supported by a Simons LSRF fellowship (J.M.), the Japan Society for the Promotion of Science (18H04136, SY), a Kwanjeong Fellowship and a Stanford Bio-X fellowship (Y.S.K.), Stanford Dean's fellowships (J.M. and T.A.M.), and an AP Giannini fellowship (T.A.M.). **Author contributions:** Y.S.K., H.E.K., S.Y., Ch.R., and K.D. initiated the opsin mining project that led to ChRmine identification, engineering, and optimization. Ch.R. prepared and transduced cell cultures, and designed all viral vectors. Y.S.K. performed opsin electrophysiology. Y.S.K. and M.I. contributed 1P opsin characterization. Y.S.K. contributed 2P opsin characterization. J.M. and K.D. initiated the MultiSLM project. J.M., S.Q., J.S., D.M., and K.D. contributed to the design, manufacturing, and characterization of the MacroSLM. S.Q. and J.M. contributed the MultiSLM optics, opto-mechanics, and control software, and built the microscope. J.M. and A.C. contributed animal surgery protocols. J.M. and S.Q. contributed in vivo MultiSLM characterization experiments. J.M. and K.D. planned behavioral experiments with T.A.M. and S.Q. contributing. J.M., Ce.R., and A.C. performed behavioral training. Ce.R. and Ch.R. contributed the histology. J.M., T.A.M., S.Q., S.G., and K.D. analyzed behavioral and neural activity data. S.G. guided modeling and theory. T.A.M. and S.G. contributed classifier and state-space analyses. J.K., B.B., and S.G. contributed

computational network modeling and theory. J.M., Y.S.K., T.A.M., S.Q., M.I., H.E.K., B.B., J.K., S.G., and K.D. designed and prepared the figures. J.M., Y.S.K., T.A.M., S.Q., S.G., and K.D. wrote the manuscript with contributions from all authors. K.D. supervised all aspects of the work. **Competing interests:** The MultiSLM and ChRmine methods are covered in pending patent application material; all methods, protocols, clones, and sequences are freely available to nonprofit institutions and investigators. At the conclusion of the study, J.M. became a member of the Scientific Advisory Board for Bruker Fluorescence Microscopy. J.S. and D.M. are employees of BNS, manufacturer of the MacroSLM device. **Data and materials availability:** All open source software packages used in the analysis are referenced in the materials and methods. Data are available at <https://sites.google.com/stanford.edu/cortical-critical-dynamics/>. ChRmine (accession number pending) and viral vector map and sequences are available at <http://optogenetics.org/>. Full specifications for the functioning microscope designed and built at Stanford University can be obtained from the corresponding author (K.D.). Specialty commissioned parts can be obtained as follows: SLM devices can be purchased as commissioned from Boulder Nonlinear Systems, SLM relay optics can be purchased as commissioned from Special Optics, and SLM beam folding prisms can be purchased as commissioned from Edmund Optics.

## SUPPLEMENTARY MATERIALS

[science.sciencemag.org/cgi/content/full/science.aaw5202/DC1](http://science.sciencemag.org/cgi/content/full/science.aaw5202/DC1)

Materials and Methods

Supplementary Text

Figs. S1 to S19

References (58–83)

31 December 2018; accepted 2 July 2019

Published online 18 July 2019

10.1126/science.aaw5202

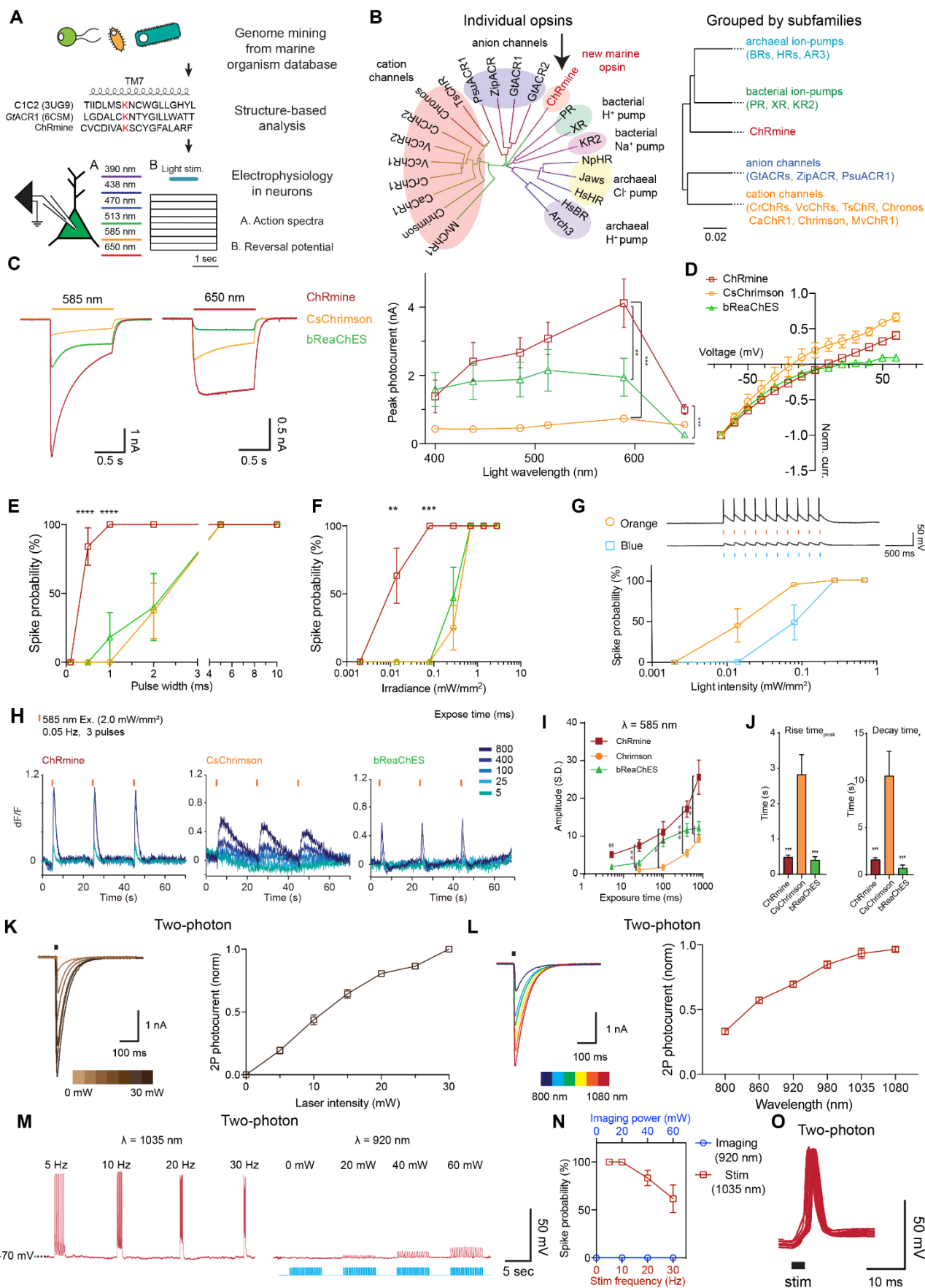




**Fig. 1. ChRmine: discovery from a marine environment of a class of opsin suitable for high-fidelity read-write experiments.** (A) Genome mining procedure. (B) Left: type-I opsin genes. Right: opsin subfamilies (scale bar denotes fractional change in amino acid sequence). (C) Left: voltage-clamp traces of red-shifted ChRs responding to 1s orange light (585 nm, 0.7 mW/mm<sup>2</sup>) or red light (650 nm, 0.7 mW/mm<sup>2</sup>) in cultured neurons. Right: action spectra in cultured neurons (0.7 mW/mm<sup>2</sup>; n=5–7 cells/condition, one-way ANOVA with Tukey correction). (D) ChR I-V curves, -70mV to +60mV, in HEK cells (n=5–7 cells/condition). (E) Spike probability vs. light pulse width (at 5Hz for 2s, 0.7mW/mm<sup>2</sup>; n=5–7 cells/condition, one-way ANOVA, Tukey correction). (F) Spike probability vs. light intensity (at 5Hz for 2s, pulse width 5ms; n=5–7 cells/condition, one-way ANOVA, Tukey correction). (G) Top: current-clamp traces. Bottom: ChRmine spike fidelity in response to orange or blue (438nm) light (n=5 cells) (H) Orange light stimulation (ticks) in cultured neurons expressing GCaMP6m and ChRmine (left), CsChrimson (middle), or bReaChES (right) at pH<sub>ext</sub>=7.4. Light pulse width varied as shown in blue shades. (I) Peak GCaMP6m responses to light pulses of varied duration [585nm light as in (H)]. (J) Trial-averaged kinetics of three opsins (n=5–7 cells/condition, one-way ANOVA, Tukey correction). (K) Two-photon power spectrum of ChRmine across 0-30mW at  $\lambda$ =1035nm. (L) Two-photon action spectrum of ChRmine (n=6 cells, 20mW, 12 rotations per spiral, 25 $\mu$ m diameter spirals, 4ms duration, 80MHz laser repetition rate). (M) Left: current-clamp trace showing spike fidelity vs. laser pulse frequency at  $\lambda$ =1035 nm. Right: spike fidelity vs. laser pulse frequency at  $\lambda$ =920 nm (2.8 Hz/frame). (N) Summary of (M), n=6 cells for stimulation and n=5 for imaging. (O) Jitter across 10 overlaid 2P-elicited ChRmine spikes (aligned to 2P stimulus timing;  $\lambda$ =1035 nm, 20mW, 12 rotations, 4ms exposure). All plots show mean $\pm$ s.e.m. unless noted. \*p<0.05, \*\*p<0.01, \*\*\*p<0.001, \*\*\*\*p<0.0001.

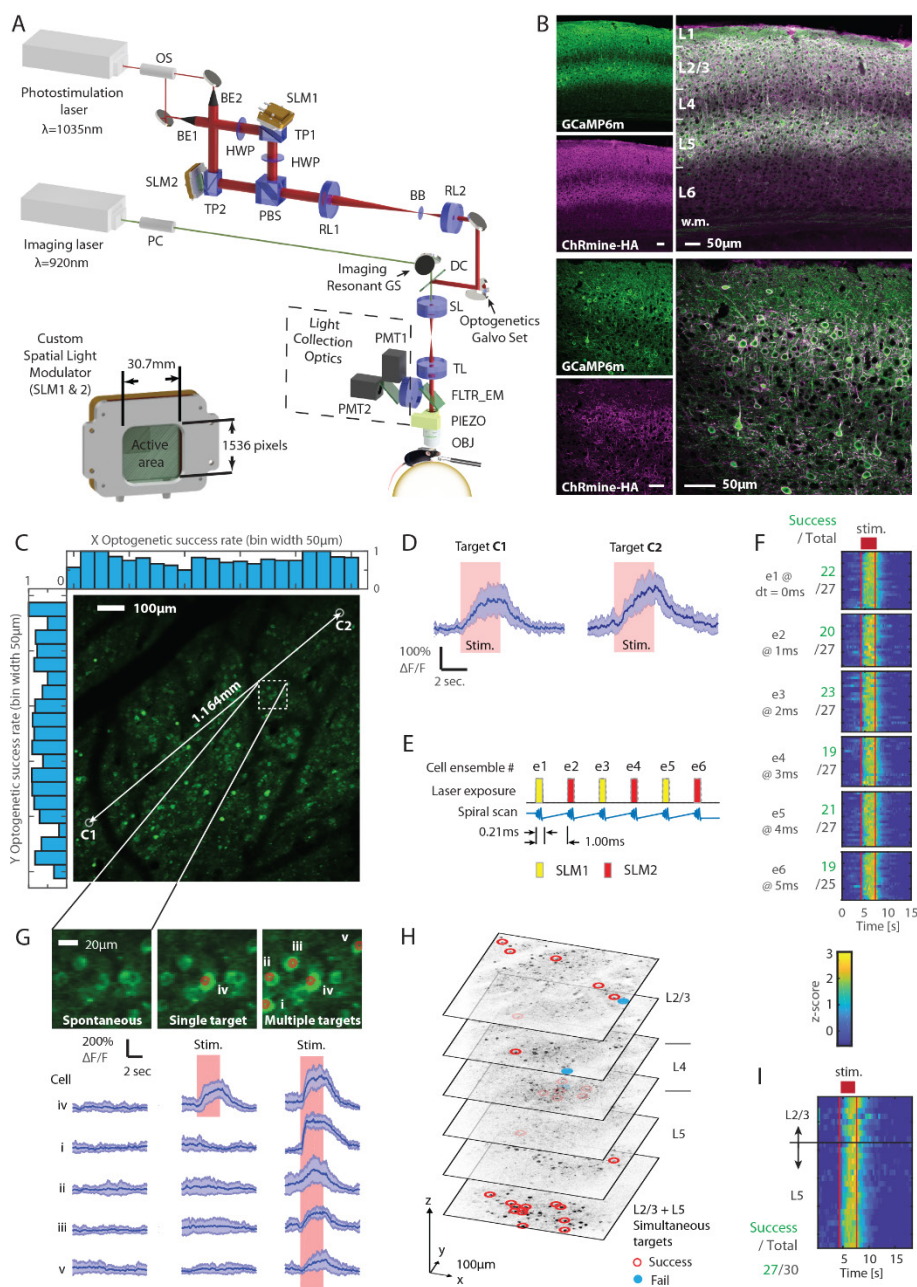


**Fig. 2. MultiSLM: large-volume temporally-precise all-optical microscope.** (A) Custom multi-photon 3D imaging and optogenetic stimulation microscope (MultiSLM). Inset: large field-of-view spatial light modulator (MacroSLM). (B) Neurons expressing both GCaMP6m and ChRmine from a single bicistronic virus (green: anti-GFP; magenta: anti-HA, as HA is conjugated to ChRmine-TS-Kv2.1; co-expression observed in 610/610 soma across nine 40  $\mu\text{m}$  V1 sections from  $n=3$  mice). (C) Simultaneous imaging and photoexcitation across a  $1\text{mm}^2$  field-of-view (160 total targets in 6 groups of neurons, 90 stimulation pulses at 29Hz, 20-30mW per target, 10 $\mu\text{m}$  diameter, 5 revolutions). (D) Photostimulation of 2 cells (identified as C1 and C2, mean $\pm$ SD), separated by 1.164mm. (E) Temporal interleaving paradigm for high-speed photostimulation of multiple neural ensembles. (F) Six nonoverlapping ensembles of 25-27 neurons stimulated every 1ms, in a 1kHz sequence (in total, 124/160 cells were successfully targeted at this speed in 5.2ms, success criteria:  $\mu_{\text{stim}} - \mu_{\text{baseline}} > 2\sigma_{\text{baseline}}$ ). (G) Targeting precision; a single neuron (target iv) can be stimulated in isolation (middle column), or within an ensemble targeted on other trials (right column); Images share common colorscale and activity traces are mean $\pm$ SD. (H) 3D imaging with simultaneous optogenetic control across cortical layers; ROI labels are enlarged for visualization. (I) Simultaneous excitation of 27/30 total targets located across cortical layers 2/3 and 5 in V1 (30 total targets, 90 stimulation pulses at 30Hz, 10-20mW/target, single 0.63ms exposure, 15 $\mu\text{m}$  diameter spiral, 8 revolutions). Note (F) and (I) on common z-score scale.

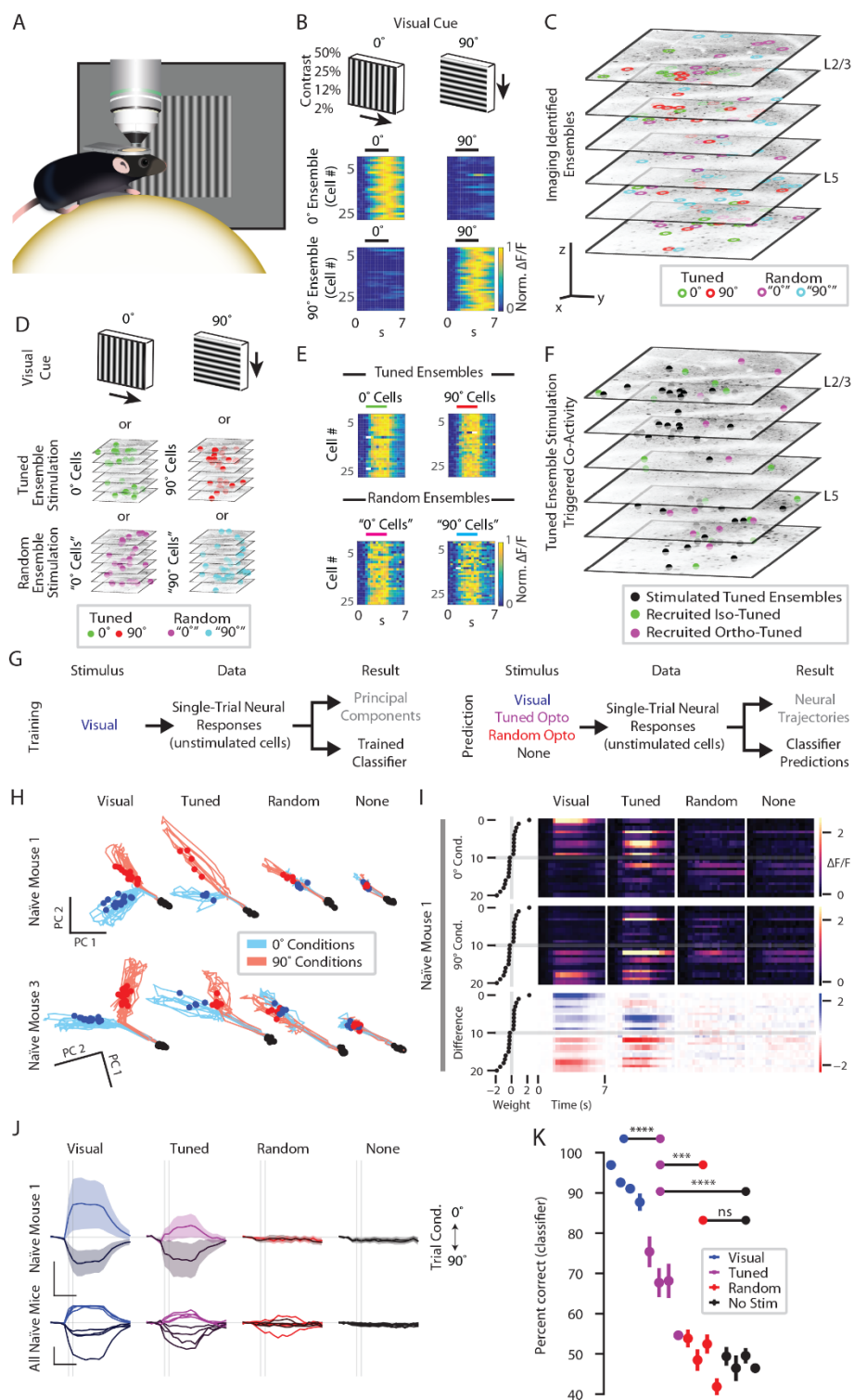




**Fig. 3. Selective visual network recruitment by functionally-defined-ensemble stimulation.** (A) Schematic of experimental apparatus. (B) Top: visual stimuli. Bottom: neural responses to visual stimuli were used to define tuned ensembles for optogenetic stimulation. (C) Spatial location of neuronal ensembles identified for stimulation. There are two tuned ensembles (green, 0° cells, red, 90° cells) and size-matched random ensembles (magenta, “0°” cells, cyan, “90°” cells). (D) Following ensemble identification, each group was stimulated without a visual stimulus present (0% contrast). Ensemble stimulation trials were randomly interleaved alongside visual stimulus trials without optogenetic stimulation. (E) Mean normalized  $\text{Ca}^{2+}$  responses for all neurons within each selective or random ensemble during optogenetic stimulation trials (red or gray horizontal bars indicates stimulation time). (F) Locations of tuned neurons stimulated and recruited for one experimental session overlaid on average images from each imaging plane through the volume. (G) Classifier and neural trajectory analysis scheme. (H) Unstimulated neurons from different experimental conditions (visual-only, tuned-optogenetic only, random-optogenetic only, or no stimulation) projected into Principal Component (PC) space defined on visual-only data. Black dots: trial start, red and blue dots: 1st frame following visual or optogenetic stimulus onset. (I) Top two rows: Mean 0° and 90° fluorescence responses in unstimulated neurons, for one mouse. Left column shows classifier weight of each neuron. Third row: first row (0° trials) - second row (90° trials). (J) Top row: Mean fluorescence response of all neurons included in the classifier analysis during 0° (brighter lines) and 90° (darker lines) conditions multiplied by their classifier weights. Error bars are s.e.m. Bottom row: weighted mean responses for four mice. Vertical lines: time interval for training the classifier. (K) Percent correct prediction performance of classifiers trained on visual data. \*\*\* $p < 0.001$ , \*\*\*\* $p < 0.0001$ .

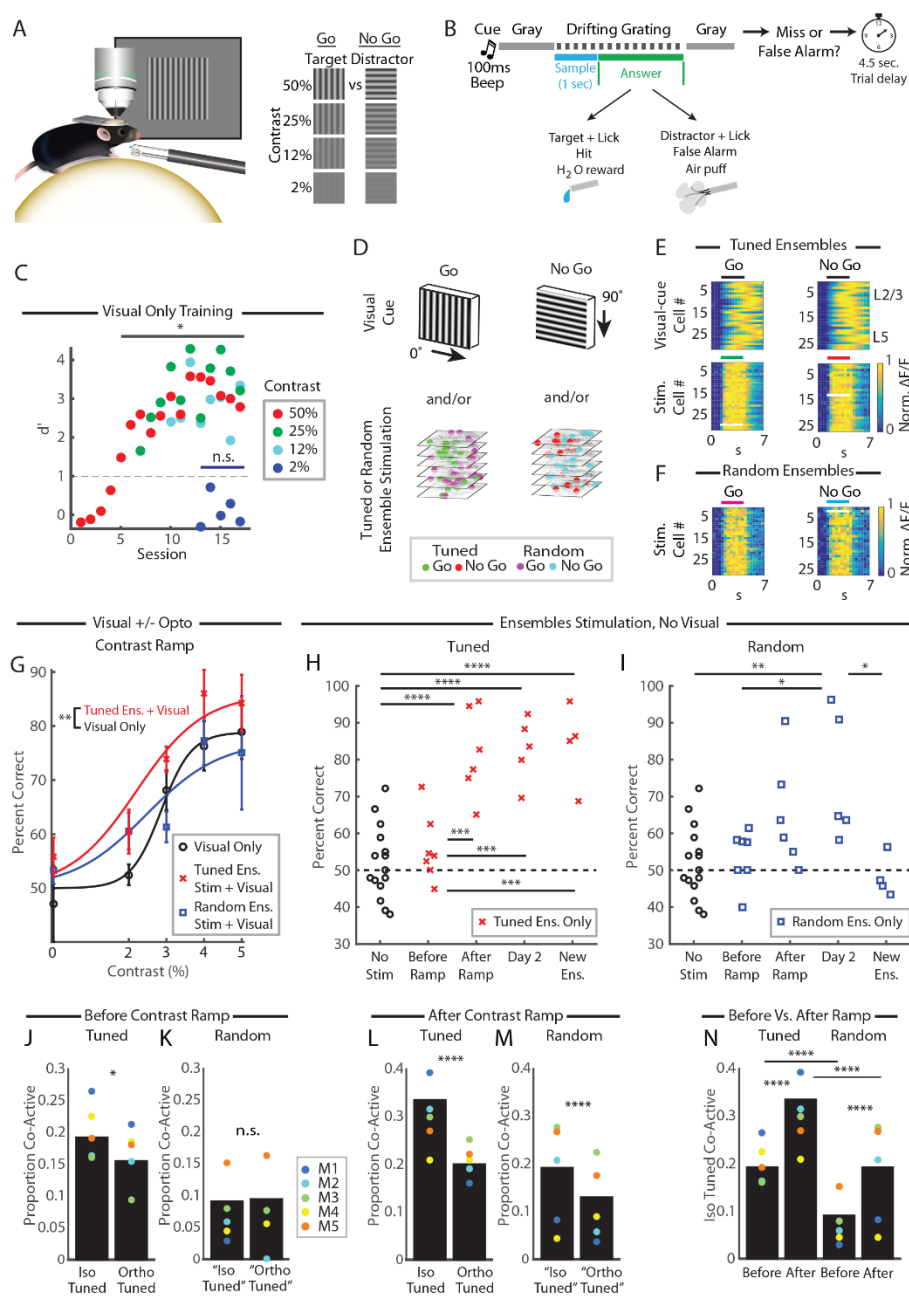


**Fig. 4. Eliciting a specific visual percept through targeting individually-identified neurons.** (A) Experimental apparatus with reward port. (B) Mice learn to discriminate vertical vs. horizontal gratings in a Go/No-Go task. (C) Visual discrimination performance of one mouse (with  $\geq 12\%$  contrast,  $p < 0.05$  Fisher's exact tests, Target vs. Distractor conditions for each session). (D) Chosen neural ensembles were stimulated alone and/or with visual stimuli. (E and F) Top row: normalized mean visual responses (50% contrast) for Target ( $0^\circ$ ) and Distractor ( $90^\circ$ ) selective ensembles. Bottom two rows: optogenetic responses for neurons within tuned (E) and random ensembles (F). (G) Discrimination performance during visual stimuli alone (black), paired with stimulation of random ensembles (blue), or with tuned ensembles (red), ( $p < 0.05$ , two-way ANOVA, main effect of stimulation type,  $p < 0.01$  tuned and visual stimulation vs. visual only, Tukey HSD,  $n = 6$  mice). Logit fits for visualization purposes only. (H) Discrimination performance of tuned ensembles before and after the contrast ramp, the following day (Day 2; or third session for mouse that did not go through the ramp), and to new ensembles ( $p > 0.05$  all unmarked pairwise comparisons, ANOVA Tukey HSD; data from  $n = 7$  mice included for each condition based on availability of data in each mouse). (I) Format matches (H) for random ensembles ( $p > 0.05$  all unmarked pairwise comparisons; dotted lines indicate chance; tuned, random and no stimulation trials were randomly interleaved within each session; the same no stimulation data were used in both H and I). (J and K) Recruitment in held-out populations during optogenetic-only stimulation before contrast ramp training (tuned ensemble stimulation:  $p < 0.05$ ,  $\chi^2$  two-tailed test,  $n = 6$  sessions in 5 mice; random:  $p > 0.1$ ,  $\chi^2$  two-tailed test,  $n = 6$  sessions in 5 mice). (L and M) Held-out recruitment during optogenetic stimulation after contrast ramp training (tuned:  $p < 0.0001$ , iso- vs orthogonally-tuned,  $\chi^2$  two-tailed test,  $n = 15$  sessions in 5 mice; random:  $p < 0.0001$ ,  $\chi^2$  two-tailed test,  $n = 13$  sessions in 5 mice). (N) Held-out iso-tuned recruitment during optogenetic stimulation after vs. before contrast ramp for tuned and random ensembles ( $p < 0.0001$ , all  $\chi^2$  two-tailed). \* $p < 0.05$ , \*\* $p < 0.01$ , \*\*\*\* $p < 0.0001$ , error bars mean  $\pm$  s.e.m. throughout.

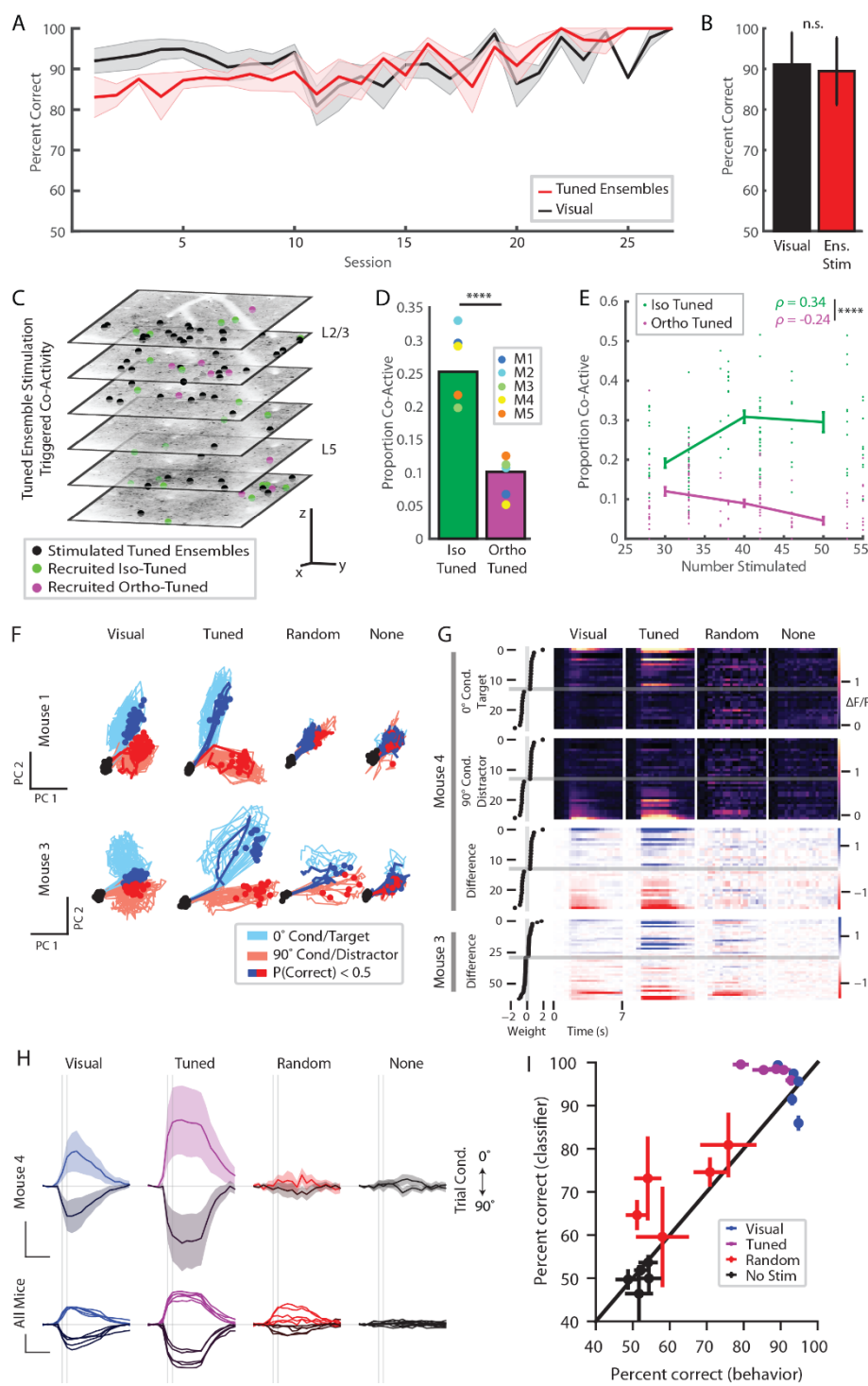




**Fig. 5. Dynamics of tuned and behaviorally potent visual ensembles.**

(A) Discrimination performance during visual only stimulation (black) and tuned-ensemble stimulation (red) over several weeks (mean $\pm$ s.e.m. for up to 5 mice per timepoint). (B) Discrimination performance for tuned-ensemble stimulation vs. visual trials (12% visual contrast behavior shown, left,  $p>0.1$  paired  $t$  test, two-tailed,  $n=112$  sessions across 5 mice; error bars s.d.). (C) Locations of tuned neurons stimulated and held-out recruited neurons for one experimental session (scale bars 100 $\mu$ m). (D) Recruitment in held-out populations during optogenetic-only stimulation across all experimental days ( $p<0.0001$ ,  $\chi^2$  two-tailed test;  $n=58$  sessions in 5 mice; mice are different colored dots). (E) Recruitment in held-out populations as differently-sized ensembles were stimulated ( $n=232$  data points from 58 sessions in 5 mice; isotuned in green, mean $\pm$ s.e.m., Spearman's  $\rho=0.34$ ,  $p<0.001$ ,  $n=116$ ; ortho-tuned in magenta, mean $\pm$ s.e.m., Spearman's  $\rho=-0.24$ ,  $p<0.01$ ,  $n=116$ ). (F) Unstimulated neurons from different experimental conditions (visual-only, tuned-optogenetic only, random-optogenetic only, or no stimulation) projected into Principal Component (PC) space defined on visual-only data. Black dots: trial start, red and blue dots: 1st frame following visual or optogenetic stimulus onset. Dark, bold trajectories denote conditions with erroneous licking behavior on average. (G) Top two rows: Mean target and distractor fluorescence responses in unstimulated neurons, for one mouse. Left column shows classifier weight of each neuron. Third row: first row (target trials) - second row (distractor trials). Bottom row: results from another mouse. (H) Top row: Mean fluorescence response of all neurons included in the classifier analysis during 0° (brighter lines) and 90° (darker lines) conditions multiplied by their classifier weights. Error bars s.e.m. Bottom row: weighted mean responses for all five mice. Vertical bars: time interval for training the classifier. (I) Behavioral performance vs. decoding performance of classifiers trained on visual-only data. Error bars: s.e.m. across sessions.

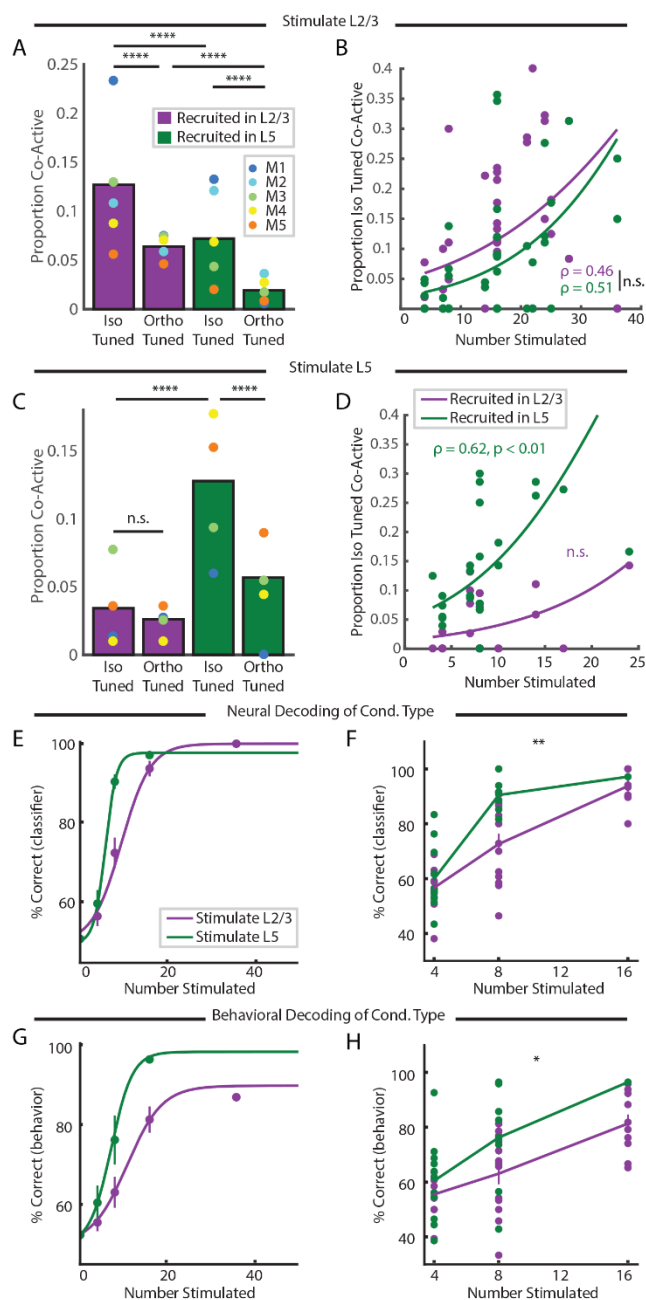


**Fig. 6. Circuit architecture underlying layer-specific perceptual thresholds.** (A) Recruitment in held-out populations during optogenetic stimulation of only tuned layer 2/3 neurons ( $\chi^2$  two-tailed test results shown). (B) Recruitment in held-out populations as a function of the number of layer 2/3 neurons stimulated (Spearman's  $\rho = 0.46$ ,  $p < 0.001$  for layer 2/3, Spearman's  $\rho = 0.51$ ,  $p > 0.1$ , Fisher z transformation comparing  $\rho$  values; function fits for visualization only). (C and D) Format matches (A) and (B) but during stimulation of only tuned layer 5 neurons. (E and G) Psychometric functions fit to predictions derived from classifiers trained on either neural or behavioral data pooled over five mice. (F and H) Data from panels (E) and (G) re-plotted for ensemble sizes used to compute two-way ANOVA results, where comparable numbers of neurons were stimulated ( $p < 0.01$  for classifier data,  $p = 0.023$  for behavioral data, main effect of layer). \* $p < 0.05$ , \*\* $p < 0.01$ , \*\*\* $p < 0.001$ , \*\*\*\* $p < 0.0001$ .

## Cortical layer-specific critical dynamics triggering perception

James H. Marshel, Yoon Seok Kim, Timothy A. Machado, Sean Quirin, Brandon Benson, Jonathan Kadmon, Cephra Raja, Adelaida Chibukhchyan, Charu Ramakrishnan, Masatoshi Inoue, Janelle C. Shane, Douglas J. McKnight, Susumu Yoshizawa, Hideaki E. Kato, Surya Ganguli and Karl Deisseroth

published online July 18, 2019

### ARTICLE TOOLS

<http://science.sciencemag.org/content/early/2019/07/17/science.aaw5202>

### SUPPLEMENTARY MATERIALS

<http://science.sciencemag.org/content/suppl/2019/07/17/science.aaw5202.DC1>

### RELATED CONTENT

<http://science.sciencemag.org/content/sci/365/6450/209.full>

### REFERENCES

This article cites 77 articles, 12 of which you can access for free  
<http://science.sciencemag.org/content/early/2019/07/17/science.aaw5202#BIBL>

### PERMISSIONS

<http://www.sciencemag.org/help/reprints-and-permissions>

Use of this article is subject to the [Terms of Service](#)